In Vitro Traumatic Brain Injury and Neurodegeneration

A DISSERTATION
SUBMITTED TO THE FACULTY OF
THE UNIVERSITY OF MINNESOTA
BY

Nicholas J. Braun

IN PARTIAL FULFILLMENT OF THE REQUIREMENTS
FOR THE DEFREES OF
DOCTOR OF PHILOSOPHY

Advisor: Dr. Patrick W. Alford

March 2021

Acknowledgements

I am indebted to Dr. Dezhi Liao, Peter Teravskis, and Dr. Bal Singh for the countless hours they spent explaining to me how neuroscience works. Thank you to Katherine Yao for being an awesome undergraduate assistant on this project. I would also like to thank the rest of my thesis committee members for their time and guidance: Dr. Brenda Ogle, Dr. Tay Netoff, and Dr. Marija Cvetanovic.

I have to acknowledge how lucky I am to have ended up in Dr. Patrick Alford's lab. Pat, you struck the perfect balance of "professor who needs his students to be productive" with "mentor trying to get his mentees where they want to go". It didn't take me long to figure out that I didn't want to pursue a career in academia, and it was probably pretty obvious how burned out I was with this project. Not all professors are willing to let their students take internships, especially internships outside of their field of study, but you did and I was better off because of it. Your commitment to my professional development in grad school has made me a better scientist, writer, speaker, and person.

To my Alford Lab 1.0 lab mates (Eric, Kerianne, Zaw), thank you for taking me under your collective wing from day one. Having three salty grad school veterans to bother with questions really made for an easy transition into the lab. To Alford Lab 2.0 (Elizabeth, Bernie, Taylor, Sam), it was a pleasure being your mother goose for the end of my tenure. I'll miss our A/V struggles during lab meeting and (Pat don't read this) I'll miss taking two-hour lunches in the breakroom.

Finally, I'd like to thank all of my family and friends. I'm stupidly fortunate to have the family that I do, and this wouldn't have been possible without their support for me every step of the way. Thank you to my fellow graduate students for the commiseration

and friendship, and thank you to my non-grad school friends for always motivating me to join your well-paid and easy-going ranks. Lastly, to my little Minnesotan family: Archie, thank you for being such a good dog and greeting me like a celebrity every time I came home after a rough day. Madison, thank you for your patience and support, and for totally entertaining my overly-dramatic “I’m gonna quit! I don’t need this!” rants every couple of months. You are the best.

Abstract

Chronic traumatic encephalopathy (CTE) is a neurodegenerative disease associated with repeated traumatic brain injury (TBI). CTE is characterized by an assortment of cognitive and behavioral changes or deficiencies, but its diagnosis can only be confirmed upon autopsy by the presence of neurofibrillary tangles (NFTs) of the protein tau in patients' brains. While CTE is not the only neurodegenerative disease in which tau accumulates in NFTs, it is unique with respect to the localization of NFTs within the architecture of the brain. In CTE, NFTs tend to cluster in the sulcal depths of the brain or in perivascular regions surrounding blood vessels, as opposed to a more diffuse dispersion of NFTs in the brain, as seen in Alzheimer's disease.

In this work, using computational modeling, we find that the preferred localization of NFTs within the sulcal depths and perivascular regions of CTE patient brains are a result of high deformation during TBI. We provide direct evidence that cell-scale mechanical deformation can elicit tau pathologies and functional synaptic deficits in neurons. The mechanical energy associated with these deformations alone can induce tau mislocalization to dendritic spines in primary hippocampal neurons harvested from neonatal rat pups. These cell-scale changes are mediated by hyperphosphorylation of tau and can be reversed with a genetic tau deletion or through the pharmacological inhibition of GSK3β and CDK5 kinases before injury.

Additionally, we investigate the role that neuronal architecture within the brain plays in determining the tauopathic and functional synaptic consequences of TBI. Using a standard viscoelastic solid material model and an image-based quantification of neuronal orientation, we correlated the work density in a neuron during a TBI simulation with

experimentally-derived tau mislocalization quantifications. Taken together, the results of this work represent an important step forward in the understanding of the cell-scale consequences of TBI, while also providing a potential therapeutic pathway for the prevention of long-term neurodegenerative consequences of TBI.

Table of Contents

List of Figures

List of Abbreviations

AD – Alzheimer's Disease

ACSF – Artificial Cerebrospinal Fluid

AMPAR – α-amino-3-hydroxy-5-methyl-4-isoxazolepropionic acid receptor

ANOVA – Analysis of Variance

APV – (2R)-amino-5-phosphonovaleric acid

CBP – CREB-Binding Protein

CTE- Chronic Traumatic Encephalopathy

CDK5 – Cyclin Dependent Kinase 5

DIV – Days *In Vitro*

DMSO – Dimethyl Sulfoxide

FTD – Frontotemporal Dementia

FTDP-17 – Frontotemporal Dementia with Parkinsonism-17

GFP – Green Fluorescent Protein

GSK3β – Glycogen synthase kinase 3 beta

HEPES – 4-(2-hydroxyethyl)-1-piperazineethanesulfonic acid

KO – Knock Out

mEPSC – miniature Excitatory Post-Synaptic Current

NFT – Neurofibrillary Tangle

PDMS – Polydimethylsiloxane

WT – Wild Type

TBI – Traumatic Brain Injury

TTX – Tetrodotoxin

Chapter 1. Introduction

1.1 Significance

TBI has become a critical public health concern due to an increased awareness of its potential to cause long-term neurological deficits. It is estimated that there are 1.6 to 3.8 million TBIs in the US annually and 5.3 million Americans are living with a disability stemming from a TBI (1–4). The most common causes of TBI are falls, being struck by an object, and motor vehicle crashes, but much of the current interest in TBI is due to observations of long-term neurodegenerative pathologies in athletes and Armed Forces servicemembers and veterans (1). The emergence of CTE diagnoses upon autopsy of former professional athletes provides a link between long-term repetitive TBI and memory deficits, behavioral changes, and neurodegenerative traits (5–9). Combat-related TBI incidence has risen in recent years due to the widespread use of improvised explosive devices in current theatres of war(10–12). TBI during a servicemember's most recent deployment is the strongest predictor of post-deployment post-traumatic stress disorder (13, 14). Additionally, servicemembers who survive TBI are significantly more at risk for AD, Parkinson's Disease, amyotrophic lateral sclerosis, CTE, and frontotemporal dementia **(**FTD) (15–20). Although the cognitive effects of CTE and its gross pathology have been well-documented, there is still a limited understanding of the mechanism of TBI injury at the cellular level (8, 11, 15).

1.2 Traumatic brain injury

TBI is characterized by the mechanism of injury; blast TBI, closed head TBI, and penetrating TBI in which an object penetrates the skull and physically lacerates brain tissue. Here, we will focus on blast and closed head TBI. In blast TBI, pressure waves that encounter the human body reflect from it and diffract around it, creating complex and non-uniform elastic and shear deformations throughout the body and brain (21, 22). Closed head TBI damage is mainly caused by the brain impacting the inside of the skull due to rapid acceleration or deceleration of the head. The human brain is protected by several membranes, and is also suspended in cerebrospinal fluid within the skull to cushion against impacts, but brain deformations and stress/strain/shear are typically caused by a single compressive force on the outer brain surface (23). This compressive force obviously causes compression, but due to the brain's incompressibility on short timescales, tensional and shear forces are also created, and are much more damaging (21, 24). Although there is no consensus on the mechanism, it is agreed upon in the brain injury field that sustaining multiple concussions puts patients at risk for longer recovery times, worsened symptoms, a higher risk for future concussions, and a predisposition to CTE (9, 25, 26), likely due to some combination of inflammatory, metabolic, and physical/mechanical damage in the brain (23, 27, 28)

1.3 Neurons

Neurons are signal transmission cells in the nervous system tasked with receiving input signals and transmitting output signals both chemically and electrically. Neurons typically consist of a cell body or soma, an axon for transmitting signals, and dendrites that

receive signals from other neurons (29). Dendrites branch from the soma and form a dense dendritic tree that receives electrochemical signals from multiple other neurons (29). Dendrites are lined with button-shaped protrusions known as dendritic spines that serve as the actual location of the signal transmission, or synapse, between two neurons (30, 31). Axons transmit efferent signals from the soma. Axon shafts are insulated with myelin, a fatty sheath produced and regulated by oligodendrocytes. Another architectural feature of the brain is the highly organized neuronal organization within the cortical layers. Neurons in the cortex of the brain extend their axon projections distally, towards the superficial surface of the brain, while their cell bodies reside in deeper lying regions of the brain (32–37).

1.4 Tau mislocalization to dendritic spines

Tau is a microtubule-associated protein that plays a role in microtubule stabilization, assembly, and transport in neuronal axons (38). Tau is in highest concentration in the axon but can appear in the nucleus and dendrites. In pathological states, this distribution may change, leading to more tau in non-axonal regions (39, 40). Tau contains several Thr-Pro and Ser-Pro motifs that are targets for kinases such as cyclin-dependent kinase 5 (CDK5) and glycogen synthase kinase 3β (GSK3β) (38). In tauopathies, these proline-rich regions are often hyperphosphorylated by CDK5 and GSK3β, leading to phospho-tau aggregation and the formation of NFTs (41–43). Accumulations of phospho-tau in the dendritic spines have been documented in mouse models of AD and FTD (44). These accumulations can lead to spine loss, changes in spine morphology, and changes in neurotransmitter receptor expression (45–49). Synaptic

alterations are the principal cause of cognitive decline and memory deficits in AD and other tauopathies. AMPAR (glutamate receptors found in many post-synaptic membranes) presence and recycling at the dendritic spine are related to synaptic plasticity, memory formation, and learning (50). mEPSCs are the small excitatory currents caused by the stochastic release of a docked and primed synaptic vesicle independent of an action potential. Synapses with phospho-tau-laden dendritic spines have decreased mEPSC amplitude and frequency, indicating an altered AMPAR presence in the post-synaptic dendritic spine (48–51).

1.5 *In vitro* traumatic brain injury

A complex array of pathologies can occur in the brain during TBI. Tau pathology, cell death, diffuse axonal injury, and damage to the cerebral vasculature can contribute to the symptoms of TBI (52). Several different methods of *in vitro* TBI simulation have been investigated as a means of recapitulating the pathology seen on the macroscopic scale (53, 54). Transection of cells has been used to study penetrating TBI and brain tissue laceration injuries, but this method is only clinically relevant for a minority of TBIs (55, 56). To simulate closed-head TBI, hydrostatic pressure (57, 58), fluid shear stress (59), and compression (60) models can be utilized, but they are difficult to employ *in vitro*, as mechanical deformations can be challenging to apply, verify, and control. In transient hydro-pressure systems, pressure waves are produced by dropping weights onto a sealed chamber to replicate pressure changes during a closed-head TBI. Fluid shear models may employ spinning discs to apply shear forces to a cellular monolayer, but shear force can be variable throughout the cell population. Compression models of TBI are typically done

with a motor-driven indenter and are only feasible at the tissue scale. Shear strain and stretch injury models offer the best finite control over the mechanical deformations applied to neurons, with a caveat being that cellular injury is dependent on adhesion to the substrate being deformed (61–63). Both shear strain and stretch injury models typically utilize elastic membranes as the substrate for neuron culture. The elastic membrane is then precisely deformed by a motor, micropipette, cantilever, etc. The uniaxial stretch injury model used in this work will be subsequently described in detail in Chapter 2.5.4.

1.6 Brain tissue- and cell-scale architecture

The human brain has a complex folded appearance at the surface level. This architecture is comprised of sulci (grooves or furrows) and gyri (ridges or folds). These folds increase the surface area of the brain allowing for white matter fibers to more efficiently link different regions of the brain, and are typically found in higher-order organisms. Although similar tau pathology can be observed in CTE and AD, the location of NFTs and spatial disease progression are very different. AD pathology begins in the deep-lying nuclei of the brain, before progressing outward and becoming relatively homogenous throughout the brain (64, 65). In contrast, CTE is found most often in the frontal cortices of the brain in its earliest stages. This is not surprising, as many TBI injuries result in the brain impacting the skull in the front of the head (64, 65). Disease progression then moves inward to deeper lying brain structures (8, 64). Interestingly, NFTs densely occupy the deepest regions of sulci in the frontal cortices in CTE. They are also found to be greatly concentrated in the perivasculature of the brain, suggesting that brain architecture could be causing stress or strain concentration in these regions, heightening

injury levels relative to the rest of the brain and increasing tauopathic disease progression. NFT accumulation in the sulcal depths and in perivasculature are not observed at similar levels in AD (8, 9, 26, 64). The highly-aligned nature of neurons in the brain may influence the severity of injury caused by TBI in different regions of the brain, since applied forces may differentially affect neurons based on their orientation.

1.7 Summary

Broadly speaking, the goal of this thesis work was to characterize the effect of *in vitro* TBI simulations on neurons by investing the tau pathology and functional synaptic deficits following injury. Along the way, using finite element modelling, we demonstrated that the regions of the brain that exhibit the most histopathological signs of CTE are regions that experience high principal strain during TBI. After proposing a mechanistic pathway that links mechanical energy imparted on neurons during TBI to tau pathology, we examine the role that cellular architecture and orientation relative to the direction of injurious deformation play in determining the deleterious effects of *in vitro* TBI.

Chapter 2. Mechanical injuries of neurons induce tau mislocalization to dendritic spines and tau-dependent synaptic dysfunction

This chapter contains material published in the Proceedings of the National Academy of Sciences, reproduced from reference (66). Braun, N.J., K.R. Yao, P.W. Alford, and D. Liao. 2020. Mechanical injuries of neurons induce tau mislocalization to dendritic spines and tau-dependent synaptic dysfunction. *Proc. Natl. Acad. Sci.* 202008306.

2.1 Summary

Chronic traumatic encephalopathy (CTE) is associated with repeated traumatic brain injuries (TBI) and is characterized by cognitive decline and the presence of neurofibrillary tangles (NFTs) of the protein tau in patients' brains. Here we provide direct evidence that cell-scale mechanical deformation can elicit tau abnormalities and synaptic deficits in neurons. Using computational modeling, we find that the early pathological loci of NFTs in CTE brains are regions of high deformation during injury. The mechanical energy associated with high strain rate deformation alone can induce tau mislocalization to dendritic spines and synaptic deficits in cultured rat hippocampal neurons. These cellular changes are mediated by tau hyperphosphorylation and can be reversed through inhibition of GSK3β and CDK5 or genetic deletion of tau. Together, these findings identify a novel mechanistic pathway that directly relates mechanical deformation of neurons to a tau-mediated synaptic impairments, and provide a possibly exploitable therapeutic pathway to combat CTE.

2.2 Introduction

Traumatic brain injury (TBI) is a critical public health concern largely due to associated long-term neurological deficits. In the United States there are 1.6-3.8 million TBIs annually, and approximately 5.3 million Americans are living with a disability stemming from a TBI (1, 2, 4). A TBI is commonly caused by a fall, being struck by an object, or an automobile crash, but recent interest in TBI stems from observations of long-term neurodegenerative pathologies in former athletes and military veterans who sustained mild TBIs during their careers. Evidence of chronic traumatic encephalopathy (CTE) in autopsies of former professional athletes suggests a link between long-term repetitive TBI and memory deficits, behavioral changes, and neurodegenerative symptoms (5–9). Service members who survive a TBI are significantly more likely to develop CTE, Alzheimer's disease (AD), and frontotemporal dementia (FTD) (15–20), all of which are neurodegenerative diseases classified as tauopathies, which are characterized by deposits of pathological forms of the protein tau in the brains of the patients. Though CTE brains contain tau pathologies that are similar to those in AD and FTD, no published studies have provided direct experimental evidence linking mechanical deformation of neurons to tau-mediated functional deficits at a cellular level.

Tau is a microtubule-associated protein that is highly concentrated in the axons of healthy central nervous system neurons (67). Tau's functions include uniformly spacing parallel microtubules and preventing microtubule depolymerization (68, 69). In some tauopathy models, disease-state tau has been shown to interfere with molecular pathways in axonal transport and the release of synaptic vesicles, and mislocalize to the neuronal soma, dendrites, and dendritic spines, resulting in synaptic impairment (48, 49, 51, 70–73).

Post-translational modifications of soluble tau, including phosphorylation by proline-directed kinases (8), phosphorylation triggered by unfolded protein response (25), cleavage by capsase-2 (74), and acetylation by CBP (11, 12), have been associated with memory deficits, synaptic dysfunction and the mislocalization of tau to dendritic spines. This mislocalization of tau has been shown to mediate synaptic dysfunction in the neuronal models of both AD and FTDP-17 (49, 51, 72). Shared tau pathology and cognitive deficits observed in CTE and other tauopathies encouraged us to elucidate the consequences of TBI on the cellular scale.

Here, we report a novel *in vitro* tauopathy model of TBI that links neuron-scale mechanical deformations to tau abnormalities and synaptic deficits in cultured hippocampal rat neurons. Using our *in vitro* TBI system, we found that high strain rate mechanical deformation alone can induce tau mislocalization and tau phosphorylation-dependent synaptic dysfunction. The tau abnormalities and synaptic deficits were shown to be preventable by inhibition of CDK5 and GSK3β, which are two widely-studied kinases that phosphorylate tau. They can also be ameliorated by genetic deletion of tau. The present study provides the first experimental evidence that directly links mechanical injury to tau-mediated synaptic deficits. The rescuing of synaptic impairments by the inhibition of tau mislocalization to dendritic spines may represent a new therapeutic strategy to prevent CTE and other neurodegenerative diseases in patients afflicted with TBI.

2.3 Results

2.3.1 High strains in brain tissue are correlated with CTE pathological hallmarks

In tauopathies, phosphorylated tau (p-tau) accumulates into dense aggregates called neurofibrillary tangles (NFTs)(75). While NFTs are a common pathophysiological hallmark of tauopathies, their distribution throughout the brain differs between diseases. In CTE, p-tau NFTs primarily aggregate in superficial cortical layers, sulci, and perivascular regions (Figure 2.1 A) (8, 9, 15, 26, 76–78). This is in contrast to other tauopathies like AD, in which NFT localization is more uniformly distributed in the deeper-lying cortical layers and not concentrated in sulcal depths or perivasculature (78). To determine the relationship between mechanical deformation of the brain and the occurrence of CTE hallmarks, we created 2D, quasi-static, finite-element models of a sulcus and microvessel during impact injury. First, depression of a rigid impactor on a geometrically symmetric sulcus was simulated, mimicking contact between the brain and skull during TBI. During impact, the model indicated that the first principal strains were largest in the sulcal depths and that the largest strains were positive, meaning the tissue was being stretched (Figure 2.1 B-E). These results were consistent with previous whole-brain models (79). Though the magnitude of the strain varied with sulcus geometry, the peak strain consistently occurred in the depth of the sulcus (Figure 2.1 D-E, Figure 2.2). Next, depression of brain tissue surrounding a pressurized microvessel was simulated. This model demonstrated that the largest strains occur immediately around the vessel and that this effect is exaggerated in smaller vessels and when the vessel modulus is stiff compared to the brain modulus (Figure 2.1 F-H, Figure 2.3). These results suggest a correlation between mechanical

deformation and tau pathology in CTE patients, and that mechanical stretching can be used to simulate the effects of TBI in brain tissue.

2.3.2 Mechanical stretching of cultured neurons induces tau mislocalization to dendritic spines and associated synaptic deficits

To study the effect of brain deformation on tauopathy, a custom-designed stretcher (80, 81) was used to apply high strain rate deformation to primary hippocampal neurons seeded on an elastic membrane (Figure 2.4 A-B). Previous studies have shown that tau mislocalizes to dendritic spines in models of neurodegenerative disease (48, 49, 51, 72), so we sought to track its localization in neurons following stretch-induced injury using neurons that were co-transfected with DsRed and WT-tau-GFP plasmids to allow for identification of dendritic spines and tau (Figure 2.4 C-D). In unstretched controls, approximately 20% of dendritic spines had a detectable tau presence. In neurons exposed to a single stretch of 20% strain (ε), at a strain rate ($\dot{\varepsilon}$) of 1000%/s, we found significant tau mislocalization to dendritic spines 24 hours post-stretch (Figure 2.4 D-E), with no significant decrease in dendritic spine density (Figure 2.4 F), demonstrating that stretch-injury can drive tau pathology *in vitro*. These injury parameters were comparable to strains and strain rates gathered from *in vivo* models of TBI (82). Tau mislocalization to dendritic spines was further verified using immunocytochemistry, which showed that both transfected WT-Tau-GFP and endogenous tau were increased in mushroom-like structures that are co-localized with/attached to Synaptophysin, a synaptic marker, after a mechanical injury to neurons (Figure 2.5 and Figure 2.6). Additionally, (in this experiment and all following tau mislocalization experiments) no relationship was seen between observed tau

mislocalization and the ratio of DsRed:GFP fluorescent intensity, indicating that variations in fluorescent protein expression levels do not explain tau mislocalization (Figure 2.7). This tau mislocalization is consistent with that seen in other tauopathy models, such as FTDP-17 and AD (48, 49, 51, 72), further supporting a role of tau mislocalization in multiple neurodegenerative diseases (24).

In FTDP-17 and AD, tau mislocalization corresponds with synaptic deficits (48, 49, 51, 72), so next we aimed to investigate whether stretch-induced tau mislocalization caused similar loss of synaptic function. We used whole-cell patch clamp to record miniature excitatory post-synaptic currents (mEPSCs) whose amplitudes and frequencies can be quantified as a proxy for synaptic health or functionality (Figure 2.4 G) (48, 49, 51, 72). Twenty four hours post-stretch (ε = 20%, $\dot{\varepsilon}$ = 1000%/s) we observed a significant decrease in mEPSC amplitude (Figure 2.4 H-I), likely indicating decreased AMPAR presence in the spines of post-synaptic neurons (83–86). We also observed decreased mEPSC frequency (Figure 2.4 J-K), suggesting a decreased release rate of neurotransmitter vesicles in pre-synaptic terminals (83–86). Tau mislocalization was found to precede electrophysiological changes in the hours immediately following stretch-injury (Figure 2.8). Taken together, these results suggest that stretch alone can induce pre- and post-synaptic functional deficiencies.

2.3.3 Tau mislocalization depends on injury dynamics

Though the exact etiology of mechanically induced tauopathy is not known, CTE is typically associated with repeated mild head injuries, not a single trauma. Thus, we sought to characterize the relationship between injury strain rate, strain magnitude, and tau

mislocalization. In neurons stretched to ε = 20% strain at varying rates of $\dot{\varepsilon}$ = 1, 10, 100, and 1000%/s, the highest strain rate stretching induced tau mislocalization, consistent with our earlier results; but at lower strain rates, we observed no significant mislocalization, when compared to controls (Figure 2.9 A-C). In neurons stretched with varying strain (ε = 1, 2, 5, 10, 20%) at a high strain rate ($\dot{\varepsilon}$ = 1000%/s), strains below 5% did not induce significant tau mislocalization, while in cells stretched 5%-20%, mislocalization increased monotonically with increasing strain magnitude (Figure 2.9 D-F). These data demonstrate the direct relationship between the dynamics of mechanical stimulus and severity of tauopathic consequences.

Brain tissue and neurons have viscoelastic material properties (87–91). The dependence of tau mislocalization on both strain and strain rate in our experiments suggests that this viscoelasticity mediates trauma-induced tauopathy. We modeled the neuron as a standard viscoelastic solid (Figure 2.9 G), with material properties based on previously published studies (91) and calculated the work done on the cell during stretching. When the work was compared to the measured tau mislocalization, we found that below 1 kJ/m^3, mislocalization did not occur; but above that threshold value, mislocalization increased monotonically with increasing work (Figure 2.9 H). This result suggests that tau mislocalization is directly related to the mechanical energy added to the neuron during trauma.

To simulate repeated trauma, we applied periodic stretches of ε = 2%, $\dot{\varepsilon}$ = 1000%/s, with one second intervals between stretches. Consistent with our previous results, a single stretch did not induce of tau mislocalization. Similarly, there was no significant mislocalization following five repetitions. However, following 10 and 20 repetitions at

small strain, we observed tau mislocalization similar to that seen in neurons exposed to a single high strain rate stretch (Figure 2.10 A-C). We applied our viscoelastic model to the repeated stretch conditions and found that mislocalization correlated with the cumulative work of the stretches (Figure 2.10 D). These data suggest that our *in vitro* and *in silico* models are able to capture some aspects of the cumulative consequences of repeated mild TBI.

2.3.4 Tau is required for stretch-induced synaptic deficits

To demonstrate that tau is required to give rise to functional deficits, we employed a Tau-KO mouse model (from Jackson Laboratory, Bar Harbor, ME; B6.129X1-*Mapt*^{tm1Hnd}/J). In three-week-old neurons harvested from TgNg control mice, a stretch injury of ε = 20%, $\dot{\varepsilon}$ = 1000%/s led to a decrease in both the amplitude and frequency of mEPSCs (Figure 2.11 A-F), consistent with our findings in rat neurons. In three-week-old neurons from Tau-KO mice, the average amplitude and frequency of mEPSCs were not statistically different from unstretched Tau-KO neurons, implying that tau pathology is necessary for functional synaptic deficits after a mechanical injury (Figure 2.11 G-L). However, when comparing the effects of mechanical injury on mEPSC characteristics in TgNg and Tau-KO neurons as a percentage difference relative to unstretched controls, it is apparent that post-synaptic processes are more affected by tau than pre-synaptic processes in our injury model (Figure 2.11 M-N). Our results show an mEPSC amplitude decrease of 17.35% in TgNg neurons compared to a small 1.02% decrease in Tau-KO neurons, indicating that post-synaptic impairment is largely tau-dependent. In contrast, mEPSC frequency was decreased by 25.78% in TgNg neurons compared to 12.58% in Tau-KO

neurons, suggesting that factors other than tau contribute to a significant portion of the pre-synaptic impairment seen after mechanical injury.

2.3.5 Stretch-induced tauopathy is mediated by tau hyperphosphorylation

CTE-associated neurofibrillary tangles are comprised of hyperphosphorylated tau (92). Thus, we next examined the role of tau hyperphosphorylation on tau mislocalization in our *in vitro* injury model. Neurons were transfected with AP tau-GFP (49), in which 14 serines(S)/threonines(T) are replaced with alanines, disallowing proline-directed phosphorylation of these residues. Following a stretch of $\varepsilon = 20\%$, $\dot{\varepsilon} = 1000\%/s$, there was minimal tau presence in dendritic spines, indicating that tau must be hyperphosphorylated at some of the 14 S/T residues to mislocalize in our *in vitro* injury model (Figure 2.12 A-C).

Next, the two main kinases responsible for hyperphosphorylating tau, GSK3β and CDK5 (41, 48, 72, 93), were inhibited with CHIR99021, Roscovitine, or both, prior to stretch. Neurons treated with either inhibitor individually showed reduced tau mislocalization, and treatment with both inhibitors concurrently further reduced mislocalization, supporting the previous findings that tau mislocalization is phosphorylation-dependent (Figure 2.12 D-F).

Finally, mEPSCs were measured in neurons treated with CHIR99021 and Roscovitine (Figure 2.13 A-L, Figure 2.14). Treatment with either inhibitor individually yielded a partial recovery of mEPSC amplitude and frequency in cells exposed to stretch. Following treatment with both inhibitors, we observed full recovery on mEPSC amplitude, and partial recovery of frequency (Figure 2.13 M-N). These results suggest that tau

mislocalization is the primary source of post-synaptic deficit in mechanically induced tauopathy, and is a contributor to pre-synaptic dysfunction, as well. These data further suggest that inhibition of tau hyperphosphorylation, can act to preserve synaptic function following stretch-injury (Figure 2.13 O).

2.4 Discussion

During TBI, the brain undergoes acute mechanical deformation at high strain rates, causing damage to neurons and glial cells (53, 93–96). This mechanical injury initiates the cascade of neurotraumatic consequences that lead to the cognitive and behavioral symptoms seen in TBI patients. In tauopathies, cognitive defects are linked to the presence of tau lesions. Unlike AD brains, in which tau lesions start at the midbrain, the earliest pathological lesions of CTE brains are deposits of p-tau aggregates in sulcal depths and perivascular regions of the cortex (64). In our computational simulation studies, we observed that maximum principal strains occur in sulcal depths and perivascular regions, supporting a mechanistic link between high strain in brain tissues, subsequent tau pathology, and the earliest lesions of CTE.

Building on these simulation results, we modeled neuronal injury using high strain rate stretching. Using this new *in vitro* model of tauopathy in TBI, we have provided the first direct cellular evidence linking mechanical stretching to tau abnormalities. We found that tau mislocalization to dendritic spines can be induced by a variety of TBI simulations, including a single large mechanical injury or multiple repetitive injuries of lesser severity. Our viscoelastic model suggests that a key determinant of the severity of tauopathy is the mechanical energy added to the neuron during deformation. Previous studies have shown

that mechanical forces can induce axonal focal swelling, akin to diffuse axonal injury observed in vivo (97, 98), and theoretical studies have suggested that the viscoelasticity of the tau protein mediates strain rate dependent collapse of microtubules in focal swellings (99). Here, we did not observe any focal swelling, but our results suggest that a similar viscoelastic mechanism plays a role in injury in sub-axonal-collapse deformations. This mechanical energy model is important for understanding injury likelihood due to dynamic loads like those caused by blast waves experienced by soldiers (11, 15), which often have complex pressure waveforms that may exacerbate injury (100, 101). In addition, this model could shed new light on the biomechanical contribution from TBI that leads to development of AD, CTE, and other tauopathies.

Our studies demonstrate the essential roles of tau hyperphosphorylation and tau mislocalization to dendritic spines in mechanical injury-induced functional deficits in excitatory synaptic transmission. We have previously reported that tau mislocalization to dendritic spines is associated with post-synaptic dysfunctions in multiple models of neurodegenerative diseases including AD (51) and FTDP-17 (49). Consistent with previous findings, here we found that the amplitudes of mEPSCs were decreased in neurons exposed to high strain-rate stretching, indicating that mechanical injuries can impair post-synaptic function by decreasing the number of AMPA receptors in dendritic spines. Mechanical stretching also decreased the frequency of mEPSCs, which may be a result of decreased releasing probability (p) and/or releasing sites (n) (102). We found no significant change in spine density, suggesting there was no change in number of synapses, and thus no change in n. Therefore, this result suggests that mechanical injuries also impair the release of pre-synaptic vesicles, likely by disrupting tau-related axonal transport.

Alternatively, the change in mEPSCs may be attributable solely to loss of AMPA receptors, as this change can reduce the number of detectable releasing sites (n) by decreasing the number of detectable active synapses and by increasing the number of "silent" synapses (103).

The signaling cascades upstream to and downstream from mechanical stretching-induced phosphorylation-dependent tau mislocalization to dendritic spines are not yet fully clarified. It has been hypothesized that, during TBI, shearing force causes extensive axonal injury and detaches tau proteins from microtubules, which subsequently causes tau hyperphosphorylation and neuronal impairment (104). The results here provide the first direct cellular evidence in support of this widely believed but not yet confirmed hypothesis. Our experiments highlight the importance of tau hyperphosphorylation in tau mislocalization (Figure 2.12 A-C), and we were able to identify potential pathways that could be exploited to mitigate some of the neurodegenerative consequences of TBI. Inhibition of both GSK3β and CDK5, two primary kinases that phosphorylate tau, reduced both the tauopathic and electrophysiological impairments of *in vitro* TBI.

Interestingly, mechanical injury-induced post-synaptic impairment is mostly blocked by genetic deletion of tau, as seen in our Tau-KO experiments. This was not true for pre-synaptic impairment, as a significant amount of pre-synaptic deficits remained in injured neurons with a genetic tau deletion (Figure 2.11). The synaptic vesicle precursors, which provide most key pre-synaptic proteins, are transported along microtubule tracks by the kinesin-3 motors (105, 106). Mechanical stretching of axons could impair axonal transport by disrupting the organization of microtubules in as little as two minutes (107). The disruption of microtubules is believed to precede the detachment of tau proteins from

microtubules and subsequent tau hyperphosphorylation (104). Therefore, it is likely that microtubule disruption caused by axonal injury may impair pre-synaptic function through tau-independent mechanisms as experimentally shown in Figure 2.11. In contrast, tau hyperphosphorylation is essential for aberrant accumulation of tau proteins in post-synaptic structures and subsequent post-synaptic dysfunction (49, 108). The blockage of most post-synaptic deficits in Tau-KO mice neurons shown in Figure 2.11 is consistent with previous tau studies (108) and supports our hypothetical model in Figure 2.13 O.

In summary, our results clearly demonstrate that the rate and magnitude of brain deformation during TBI influence tau-mediated neural injuries, providing a plausible neurobiological explanation for the formation of tau deposits in sulcal depths and perivascular regions, the two pathological hallmarks of CTE. Mechanistically, we have provided a novel molecular framework (Figure 2.13 O), by which mechanical injuries lead to tau hyperphosphorylation, tau mislocalization, and tau-dependent impairment of excitatory synaptic functions. The shared tau pathway that can be activated by TBI (shown here), AD, and FTDP-17 (49, 51) unravels a novel neurobiological basis for the high risks of AD in boxers, football players and military personnel (7–9, 15, 16). Our characterization of mechanical components associated with neuronal injuries may provide new information for future development of protective gear for soldiers and athletes and, a starting point for development of novel therapeutic strategies to target the signaling pathways involved in tau-mediated synaptic dysfunction to treat and prevent CTE.

2.5 Methods

2.5.1 Sulcus and microvessel models

Mechanical deformation in the sulcus and microvessel-surrounding tissue were simulated using COMSOL Multiphysics 4.2 (Burlington, MA). Both were modeled as 2-D plane strain bodies with linear elastic material properties, undergoing quasi-static deformation. In both models, brain tissue was treated as an isotropic linear elastic material given by

$$\sigma_{ij} = 2\mu\epsilon_{ij} + \lambda\delta_{ij}\sum_{k=1}^{3}\epsilon_{kk} \quad (1)$$

where σ_{ij} and ϵ_{ij} are the i, j components of the stress and strain tensors, respectively, δ_{ij} is a Kroneker delta, μ is the shear modulus, and λ is the first Lamé parameter. These material properties can be given in terms of the more common Young's modulus (E) and Poisson's ratio (ν) by

$$\mu = \frac{E}{\nu(1+\nu)}, \quad \lambda = \frac{E\nu}{(1+\nu)(1-2\nu)} \quad (2)$$

The material parameters were estimated based on previous studies (109) as $E = 1.895\ kPa$ and $\nu = 0.45$. In the microvessel model, the vessel wall was also treated as a linear elastic material, with a Young's modulus given as $E_{vessel} = \alpha E_{brain}$, where α is a scalar where $\alpha \geq 1$, and $\nu = 0.45$.

In the sulcus model, roller boundary conditions were applied to the side and bottom edges of the brain tissue section, and a contact pair was created between the rigid indenter and the sulcal boundary of brain tissue. Incremental displacements were prescribed to the indenter, which in turn initiated the contact between indenter and brain tissue. The volume of the intrasulcal space was not conserved, as the cerebrospinal fluid found in the sulci, *in vivo*, is free to flow out of the sulci and about the intracranial space. In the microvessel

model, a roller boundary condition was used on the bottom boundary and the top boundary was uniformly displaced. To model incompressible blood within the vessel, the volume of the lumen was conserved.

The geometry of the model was meshed with triangular elements and the parametric solver was used to determine the effects of geometry and material properties on model behavior. Parameters that were tested were the sulcal depth, sulcal width, gyral radius, sulcal radius, microvessel diameter, microvessel wall thickness, and microvessel stiffness ratio (α). In all models, the first principal strain, defined as the largest eigenvalue of the strain tensor, was calculated and the peak values within the brain tissue during deformation were reported.

2.5.2 Stretching construct preparation

High-velocity stretching constructs were prepared for cell culture by first spin-coating 0.010" thick silicone sheeting (SMI, Saginaw, MI) with a 10 μm thick layer of Sylgard 527 PDMS (Ellsworth Adhesives, Germantown, WI) at a 1:1 base to crosslinker ratio. After curing, these membranes were suspended under tension between two custom-designed metal brackets (Oakdale Precision, Saint Paul, MN), and a Sylgard 184 PDMS (Ellsworth Adhesives, Germantown, WI) ring was adhered to the membrane to contain cell culture media upon cell seeding. The constructs were treated with a UVO-Cleaner (Jelight Co. Inc., Irvine, CA) for eight minutes and then incubated in a solution of 100 μg/mL poly-D-lysine and 4 μg/mL laminin (Sigma-Aldrich, Saint Louis, MO) in a cell culture incubator overnight.

2.5.3 Cell isolation and culture

Primary hippocampal neurons were harvested from Hsd:Sprague Dawley newborn rat pups as previously described (Envigo, Indianapolis, IN) (110). Hippocampi from each pup were isolated and pooled together in ice-cold Earl's Balanced Medium supplemented with 1mM D-glucose before tissues were digested, meaning that hippocampal neurons from each pup were combined and mixed with hippocampal neurons from its litter-mates. Cells were then seeded onto the stretching constructs at a density of 10^6 cells per construct in plating media (minimal essential media with Earle's salts, 10 mM HEPES, 10 mM sodium pyruvate, 0.5 mM glutamine, 12.5 μM glutamate, 10% FBS and 0.6% glucose) (Thermo Fisher Scientific, Walthan, MA). The day of plating was denoted as day-in-vitro 1 or DIV1. Approximately 4 hours after plating, the media was replaced with fresh plating media to remove non-adherent cells and debris. 24 hours after plating, media was replaced with NbActiv1 neuron culture medium media (BrainBits, LLC, Springfield, IL). Cells were maintained in a 37°C, 5% CO_2 environment throughout the duration of the experiment. 50% media changes with NbActiv1 were performed on a weekly basis. For mouse experiments, the same cell isolation and culture protocols were followed. C57BL/6J mice (TgNg) and B6.129X1-*Mapt*^{tm1Hnd}/J mice (Tau-KO) were used (Jackson Labs, Bar Harbor, ME).

2.5.4 Simulated TBI via high-strain rate stretching

To simulate the mechanical deformations in the brain during a TBI we applied a high strain rate acute uniaxial stretch to cultured hippocampal neurons at DIV 22. A linear motor (PS01-23x80F/100x160-HP-R, LinMot USA, Elkhorn, WI) was used to displace

one end of the cell-seeded elastic substrate with fine control over both strain (ϵ) and strain rate ($\dot{\epsilon}$), to simulate injury. Single stretches were performed with $\epsilon = 0 - 20\%$ and $\dot{\epsilon} = 0 - 1000\ \%/s$. For repeated stretch experiments, stretches of $\epsilon = 2\%$ and $\dot{\epsilon} = 1000\ \%/s$ were applied in 1s intervals 1, 5, 10, or 20 times.

2.5.5 Transfection constructs

Each of the human-tau constructs was tagged with enhanced GFP (denoted as GFP) on the N-terminus, expressed in the pRK5 vector, and driven by a cytomegalovirus (CMV) promoter (Clontech, Inc., Mountain View, CA). The DsRed constructs (Clontech, Inc., Mountain View, CA) were also expressed in the pRK5 vector and driven by a CMV promoter. The WT-tau construct encoded human 4R tau lacking the N-terminal sequences (4R0N) and contained exons 1, 4 –5, 7, and 9 – 13, intron 13, and exon 14. WT-tau was used as a template to create an AP tau construct, which was generated by mutating all 14 S/P or T/P amino acid residues (T111, T153, T175, T181, S199, S202, T205, T212, T217, T231, S235, S396, S404 and S422; numbering based on the longest 441-amino acid brain isoform of htau) to alanine. The PCR-mediated site-directed mutagenesis was confirmed by sequencing.

2.5.6 Transfection and imaging

A standard calcium phosphate precipitation method was used to transfect hippocampal neurons with desired plasmids at DIV7-8 (111). Neurons were co-transfected with DsRed and either htau variant (WT or AP) at a 2:1 ratio. DsRed was used to visualize the morphology of neurons, including the location of dendritic spines. Transfected cells

were then allowed to mature for two weeks before further experimentation. 24 hr after stretch was applied, the constructs were mounted to a platform above a Nikon inverted epifluorescent microscope using a custom-designed stage attachment. All images of neurons transfected with DsRed and WT-tau or AP tau were acquired using a 40x water immersion lens and computerized focus motor starting at DIV 23. All digital images were acquired using MetaMorph Imaging System (Universal Imaging Corporation, Bedford Hills, NY) as 15-image stacks with a 0.5 micron step in the *Z* direction separating each image. Stacks were processed via MetaMorph Imaging System's 2D nearest neighbors deconvolution function before removing out-of-focus slices and averaging the stack into a single image. DsRed and WT- or AP tau images were paired and overlaid in Adobe Photoshop (Adobe Inc, San Jose, CA) in order to count dendritic spines and the presence or lack of tau in each dendritic spine. Each dendritic spine was treated as a binary event (tau present or no tau present) and the total sample population of dendritic spines was used for statistical analysis. For spine density counts, two dendrites were traced in their entirety for each acquired image, and the length recorded in microns. Dendritic spines were counted along each dendrite, and dendritic spines / 100 microns were calculated for each image, using the image average value for statistical analysis. The ratio of DsRed fluorescent intensity to GFP fluorescent intensity was calculated and recorded for each image to ensure that no results owed to erroneous fluctuations in the transfection efficiency of either plasmid. For each acquired image, the brightness of DsRed and GFP were recorded at three neural processes and then averaged. Each of these averages was used to compute group means and standard deviations. A maximum of two cells per dish were imaged for tau mislocalization imaging experiments.

2.5.7 Electrophysiology

Miniature EPSCs were recorded from hippocampal neurons at DIV 23 using 5 megaohm glass pipettes at holding potential of -55 mV(49). Recording in whole-cell configuration lasted up to 5 minutes, using an Axopatch 200B amplifier and pClamp 11 (Molecular Devices, San Jose, CA). For each second one recording sweep of 200 ms was sampled. Recordings were filtered at 1 kHz with an output gain of $\alpha = 1$. Neurons were rinsed once with artificial cerebrospinal fluid (ACSF) at room temperature containing 100 µM APV (an NMDAR antagonist), 1 µM TTX (a sodium channel blocker), and 100 µM picrotoxin (GABAa receptor antagonist), and then bathed in ACSF for electrophysiology while being gassed with 95% O_2-5% CO_2. ACSF was comprised of 119 mM NaCl, 2.5 mM KCl, 5.0 mM CaCl2, 2.5 mM MgCl2, 26.2 mM NaHCO3, 1 mM NaH2PO4 and 11 mM glucose. The patch pipette was filled with an internal solution containing 100 mM cesium gluconate, 0.2 mM EGTA, 0.5 mM $MgCl_2$, 2 mM ATP, 0.3 mM GTP, and 40 mM HEPES (pH 7.2 with CsOH) (Sigma-Aldrich, Saint Louis, MO). All mEPSCs were manually identified with the MiniAnalysis software (Synaptosoft Inc, Fort Lee, NJ) based on a threshold amplitude of 3 pA, a characteristic fast-rising phase, and a slow-decaying phase. The amplitude and frequency of all recorded and verified mEPSCs were averaged for each neuron and treated as a single sample for further statistical analysis. A maximum of one cell per dish was patched for all electrophysiology experiments.

2.5.8 Inhibition of tau hyperphosphorylation

1000X (500 mM) solutions of CHIR99021 and Roscovitine (Sigma-Aldrich, Saint Louis, MO) were made using DMSO (Sigma-Aldrich, Saint Louis, MO). The 1000X

solutions were mixed with cell media to create a 1X (500 nM) solution. Neurons were treated with CHIR99021, Roscovitine, or both drugs one hour before stretching, and the media containing drugs was left on the neurons throughout the remaining duration of experiments.

2.5.9 Immunocytochemistry

Cultured neurons were fixed and permeabilized with 4% paraformaldehyde + 4% sucrose (23°C, 30 min), 100% methanol (–20°C at the beginning, incubated at 23°C for 20 min), and 0.2% Triton X-100 (23°C, 20 min) applied successively as previously described (68). For all immunocytochemical staining, both primary and secondary antibodies were diluted at 1:100 in 10% donkey serum in PBS. The fixed neurons were incubated with primary antibodies at room temperature overnight and subsequently incubated with rhodamine (red)- or FITC (green)-labeled secondary antibodies for 1.5 hours at room temperature. The stained cultures were mounted with a 0.8 mm thick coverslip with Permaluor Aqueous Mounting Medium (TA-030-FM, Thermofisher, Walthan, MA) and imaged with a Nikon microscope with a 63X oil objective. In Figure 2.5, neurons expressing GFP-tagged wild-type human tau proteins were incubated with a primary mouse monoclonal anti-Synaptophysin antibody (MAB5258; from Millipore) and subsequently with a goat rhodamine (red)-linked secondary anti-mouse antibody to detect presynaptic terminals. Putative "functional" dendritic spines were defined as GFP-labelled mushroom-like structures (green) that are co-localized with or adjacent to a presynaptic terminal labeled by the anti-Synaptophysin antibody (red). In Figure 2.6, cultures were co-incubated with the widely used mouse monoclonal anti-tau antibody Tau-5 (sc-58860;

Santa Cruz Biotechnology, Dallas, TX) and a rabbit polyclonal anti-synaptophysin antibody (RP036; from Diagnostic Biosystems, Pleasanton CA); they were subsequently incubated with a goat secondary FITC (green)-linked anti-mouse antibody and a goat secondary Rhodamine (red)-linked anti-rabbit antibody to detect endogenous tau and presynaptic terminals, respectively. For Synaptophysin cluster density counts, two neurites were traced in their entirety for each acquired image, and the length recorded in microns. Synaptophysin clusters were counted along each neurite, and clusters / 100 microns were calculated for each image, using the image average value for statistical analysis.

2.5.10 Viscoelastic neuron model

Mechanical energy added to the dendritic spine during injury was determined by calculating the work per unit volume done on the cell during stretching. Neurons have previously been shown to act as viscoelastic Kelvin solids (90), but neurites are significantly more fluid-like than the soma, and become more fluidic with increasing stress (91). To capture both of these observations, we modeled the neurite as a standard viscoelastic solid with two springs and one dashpot (Figure 2.9 G) and described by the equation

$$\frac{\dot{\sigma}}{E_1} + \frac{\sigma}{\eta_1} = \frac{E_1+E_2}{E_1}\dot{\epsilon} + \frac{E_2}{\eta_1}\epsilon \tag{3}$$

where σ is the stress, ϵ is the strain, $\dot{\sigma}$ and $\dot{\epsilon}$ are the stress and strain rates, respectively, E_1 and E_2 are the moduli of the springs and η_1 is the viscosity of the dashpot. E_1, E_2, and η_1 were determined by simulating a creep test, as performed by Grevesse et al (91), and fitting the parameters to their results using least squares fitting.

To model neurite stretching, we let ϵ and $\dot{\epsilon}$ match those applied experimentally (Figure 2.9 H) and calculated σ using Eq (3) and finite differences. The work per unit volume (w) was taken as

$$w = \int \sigma \, d\epsilon \tag{4}$$

over the period from the initiation of stretch to the time at which ϵ is at its peak value. For repeated stretch analyses, the total work was taken as the sum of the work of each stretch.

A parameter study was performed to determine how the values of $E_1, E_2, and\ \eta_1$ influence the results by setting $E_1 = \beta E_2$ and repeating the solution above for a given β (Figure 2.15).

2.5.11 Statistical analyses and reproducibility

In the case of quantifying tau mislocalization, a total number of dendritic spines and dendritic spines containing an observable tau presence (summed from all recorded images) was documented for each experimental treatment. From this, a proportion of dendritic spines containing tau was calculated for each experimental group. A Chi-squared test for multiple proportions was performed to assess whether statistical differences existed between all groups, and then two-proportion pooled z-tests were performed pairwise to determine which groups were statistically different from one another. For dendritic spine density electrophysiology, synaptophysin cluster density, and tau/synaptophysin co-localization data, one-way ANOVA was performed to test for variance between all groups, followed by a *post-hoc* Tukey test for pairwise comparisons. For cumulative frequency distributions, K-S tests were used to compare mEPSC amplitude and period distributions between unstretched controls and all treated groups. The ratio of the K-S test statistic (D)

to the statistical critical value (D_{crit}) is presented in the appropriate figure caption. All tests had statistical significance set for $\alpha = 0.05$. Chi-squared tests, two-proportion pooled z-tests, ANOVA, and Tukey tests were performed using SigmaPlot 11.0 (Systat Software Inc., San Jose, CA). K-S tests were performed using Microsoft Excel (Microsoft, Seattle, WA).

In total, tau mislocalization experiments utilized 25 different litters of rat pups, with an approximate litter size of 10-12 pups. Cells from each of these litters were transfected to asses tau mislocalization or to confirm co-localization of tau and Synaptophysin. Electrophysiology experiments required 17 litters of rat pups. For both experiments, each litter came from a different timed-pregnancy rat dam, which was euthanized after giving birth. TgNg and Tau-KO mouse pups for electrophysiology experiments were bred by us. Two males and four females of each genotype were purchased and three litters of each genotype were used for experiments. Each litter of pups had a distinct parentage to maintain genetic diversity variation within the experiment.

2.5.12 Animal usage

The breeding, handling and usage of rats and mice have been approved by the Intuitional Animal Care and Use Committee (IACUC) at the University of Minnesota (Protocol #1809-36344A). Rat pups (< 1 week old) were decapitated to harvest brain tissues strictly following the IACUC guidelines.

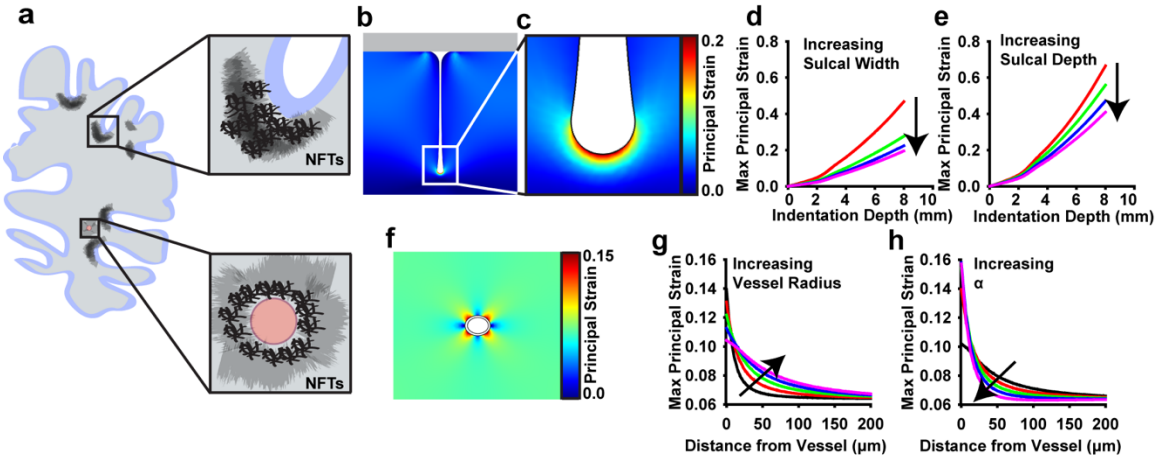

Figure 2.1 CTE-associated p-tau NFTs accumulate in regions of the brain that undergo the greatest mechanical deformation during TBI. (A) NFTs accumulate in the sulcal depths and perivascular regions of the brain in CTE patients (8). (B-C) 2D quasi-static, finite element model of a single sulcus during impact injury. First principal strain is at a maximum in the deepest part of the sulcal depth. (D-E) Parametric studies of the effect of brain geometry on maximum principal strain during impact in the sulcus model. (D) Effect of sulcal width on maximum first principal strain. (width = 5, 10, 15, 20 mm) (E) Effect of sulcal depth on maximum first principal strain. (depth = 50, 60, 70, 80 mm) (F) 2D quasi-static, finite element model of a perivascular region surrounding a single pressurized blood vessel. First principal strain is at a maximum nearest the vessel. (G-H) Parametric studies of the effect of vessel geometry and material properties on principal strain during brain deformation. (G) Effect of vessel outer radius on spatial strains. (radius = 30, 40, 50, 60, 70 mm) (H) Effect of vessel modulus on spatial strains, where $E_{vessel}=\alpha E_{brain}$. ($\alpha$ = 3, 9, 21, 41, 81).

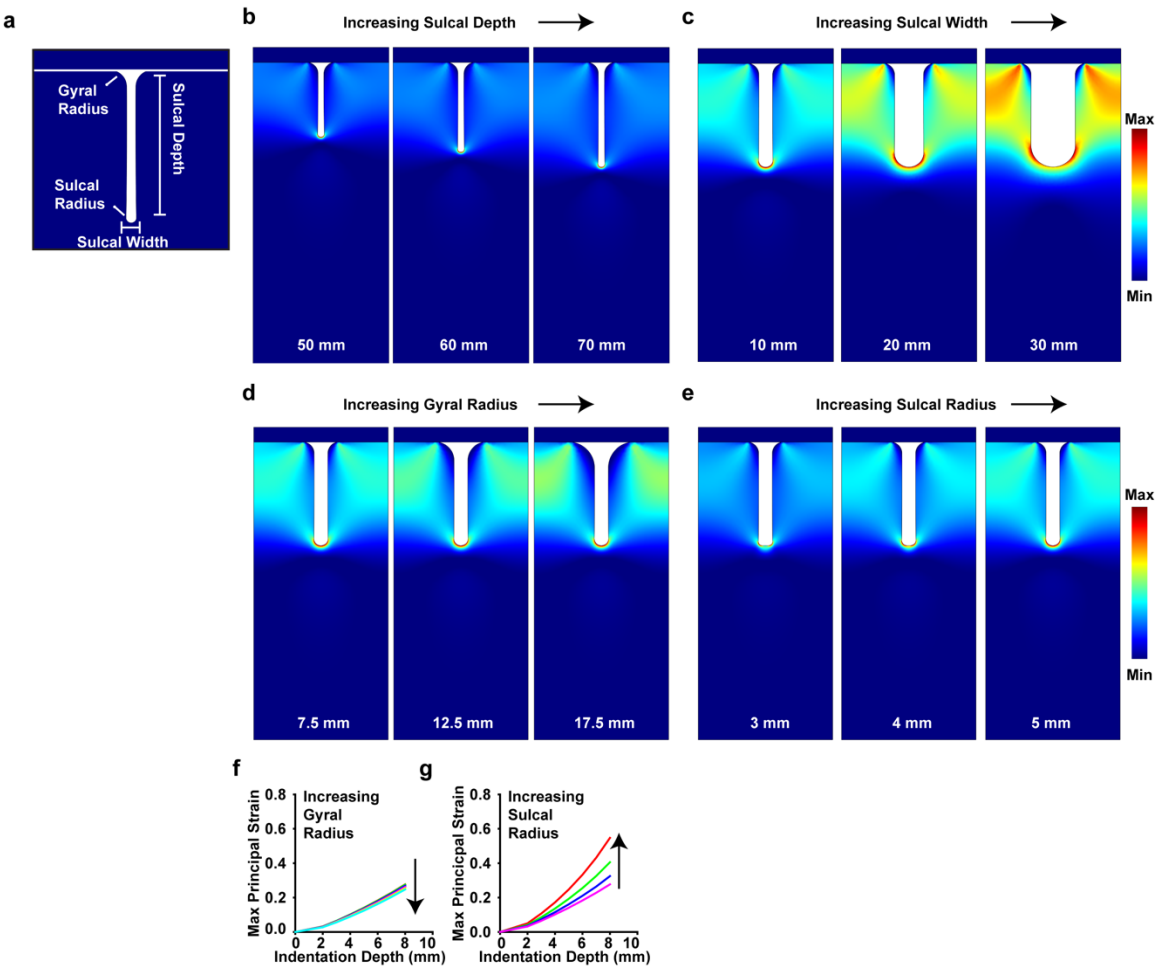

Figure 2.2 Sulcal geometry does not qualitatively affect peak strain location during impact. (A) Schematic representation of a sulcus in our 2D finite element model. (B-E) Parametric studies of the effect of sulcus geometry on spatial strain distributions. All images show impact displacement of 2 mm. Note: Heat maps scale from minimum to maximum first principal strain within the image such that image-to-image magnitudes do not correlate. (B) Varied sulcal depth. (C) Varied sulcal width. (D) Varied gyral radius. (E) Varied Sulcal radius. (F) Effect of gyral radius on maximum first principal strain (radius = 7.5, 10, 12.5, 15, 17.5, 20 mm). (G) Effect of sulcal radius on maximum first principal strain (radius = 2, 3, 4, 5 mm).

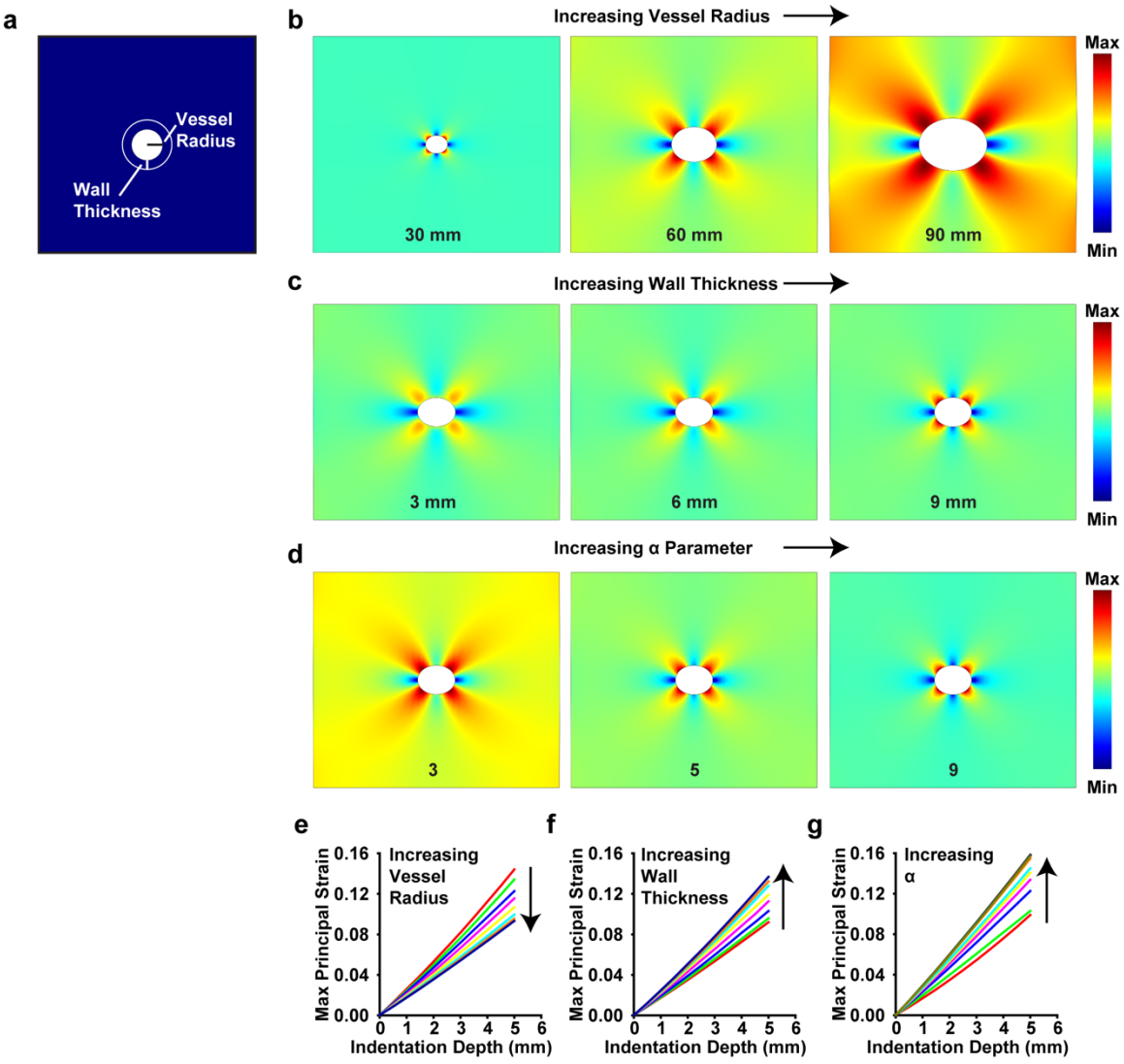

Figure 2.3 Blood vessel geometry and material properties influence strain magnitude during impact. (A) Schematic representation of the blood vessel and surrounding brain tissue in our 2D finite element model. (B-D) Parametric studies of the effect of vessel geometry and material properties on spatial strain distributions. All images show top surface displacement of 5 mm. Note: Heat maps scale from minimum to maximum first principal strain within the image such that image-to-image magnitudes do not correlate. (B) Varied vessel outer radius. (C) Varies vessel wall thickness. (D) Varied vessel wall

modulus where $E_{vessel} = \alpha E_{brain}$. (E) Effect of vessel radius on maximum principal strain (radius = 30, 40, 50, 60, 70, 80, 90, 100 mm). (F) Effect of vessel wall thickness on maximum principal strain (thickness = 2, 3, 4, 5, 6, 7, 8, 9, 10 mm). (G) Effect of vessel wall modulus on maximum principal strain (α = 1, 3, 5, 7, 9, 11, 21, 31, 41, 51, 61, 71, 81, 91).

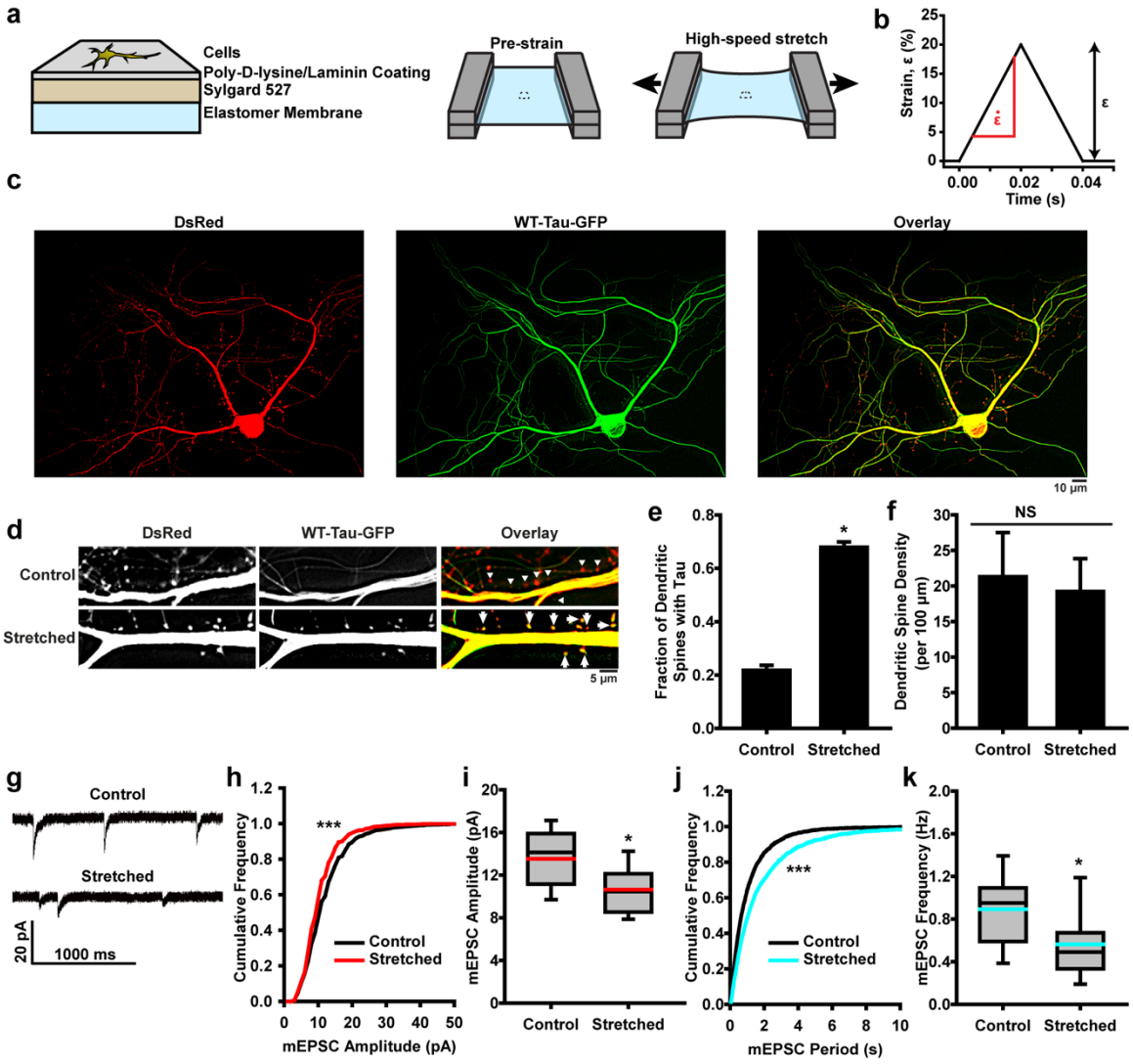

Figure 2.4 Neurons exposed to high strain rate deformation exhibit tau abnormalities and synaptic functional deficits. (A) Schematic representation of *in vitro* TBI system construct fabrication and stretching. (B) Prescribed temporal wave form for a stretch of 20% strain (ε), and 1000%/s strain rate ($\dot{\varepsilon}$). (C) Representative images of cultured rat hippocampal neurons transfected with DsRed (left), WT-Tau-GFP (center). Images overlaid to assess tau mislocalization (right). (D) Representative images of tau mislocalization in to dendritic spines in control and stretched neurons. *Arrows* denote spines with tau, *triangles* indicate spines without tau. (E) Quantification of tau

mislocalization, measured as fraction of spines with tau present, in unstretched control and stretched neurons. (mean +/- stdev). (spines/images): Control = 669/23, Stretched = 524/7. (F) Spine density in unstretched control and stretched neurons. (mean +/- stdev). (G) Representative mEPSCs recorded from unstretched control and stretched neurons. (H) Cumulative frequency of mEPSC amplitude (black: control, red: stretched), K-S test: $D/D_{crit} = 4.31$, $\alpha = 0.05$, bins = 1 pA. (I) Quantification of mEPSC amplitudes (black line: median, red: mean, box: 25%-75%, whisker: 10%-90%). (J) Cumulative frequency of mEPSC peak-to-peak period (black: control, teal: stretched), K-S test: $D/D_{crit} = 5.48$, $\alpha = 0.05$, bins = 50 ms. (K) Quantification of mEPSC frequency. (black line: median, teal: mean, box: 25%-75%, whisker: 10%-90%). (cells/mEPSCs): Control = 18/4360, Stretched = 23/3139. All plots: * denotes $P<0.05$, *** denotes $P < 0.001$ compared to control, *NS* is not significant.

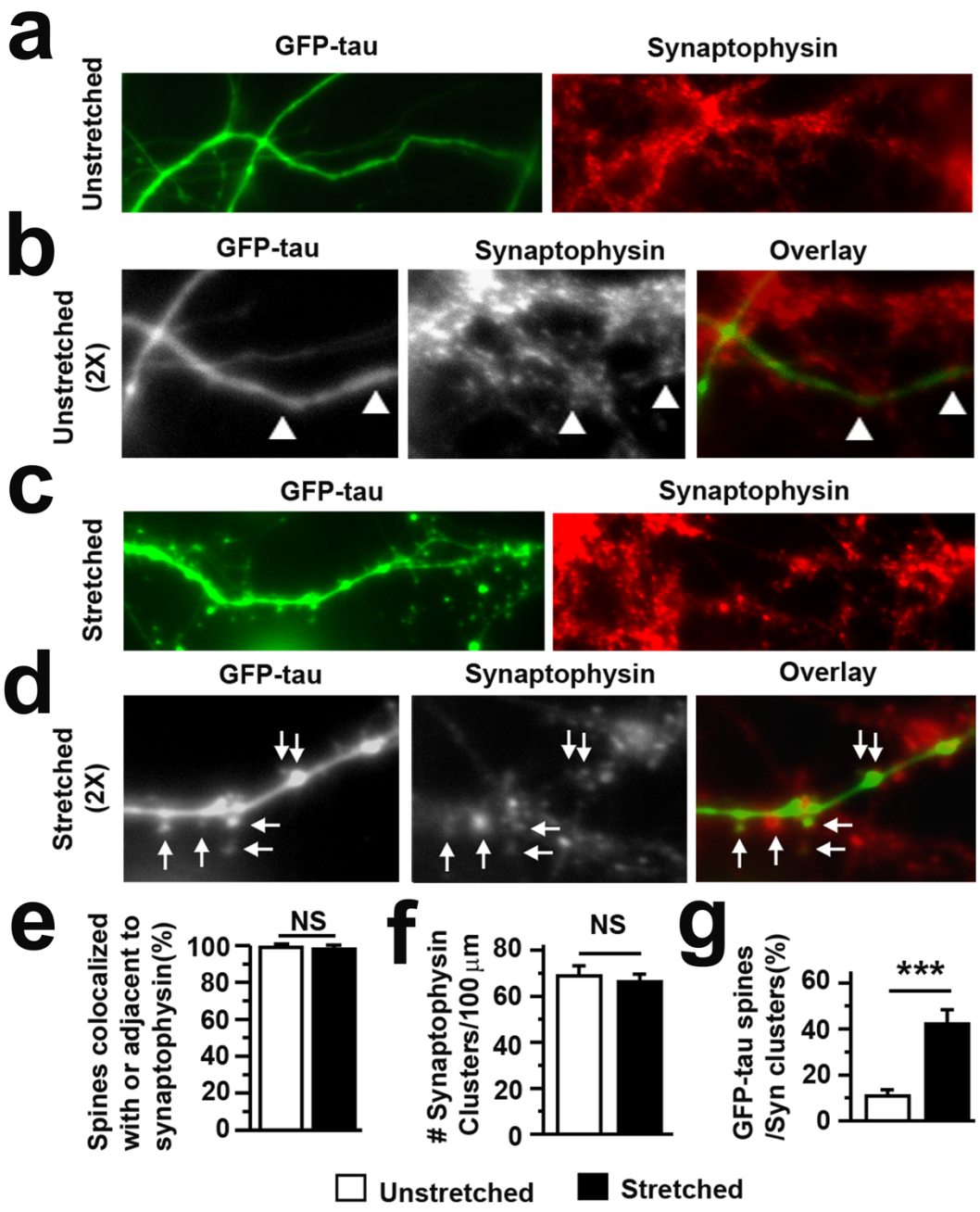

Figure 2.5 WT-Tau-GFP is present in spine-like structures that co-localizes or attached to pre-synaptic terminals following mechanical injury. (A) Unstretched neurons transfected with WT-Tau-GFP were stained with a mouse anti-Synaptophysin antibodies to label pre-synaptic terminals. (B) 2X magnification of images from (A). *Triangles* denote Synaptophysin clusters without GFP presence. (C) and (D) Similar

images as in (A) and (B) from stretched neurons. *Arrows* denote the GFP-labelled mushroom-like structures that are colocalized with or attached to Synaptophysin clusters. (E) Over 98% of GFP-labelled mushroom-like structures are colocalized with or attached to Synaptophysin clusters (mean +/- stdev). It suggests that they are likely to be functional dendritic spines. (F) Quantification of Synaptophysin cluster density along unstretched and stretched neurites. (mean +/- stdev). (G) Quantification of the percentage of Synaptophysin clusters that colocalized with/attached to GFP-tau spines over total number of Synaptophysin clusters (mean +/- stdev).

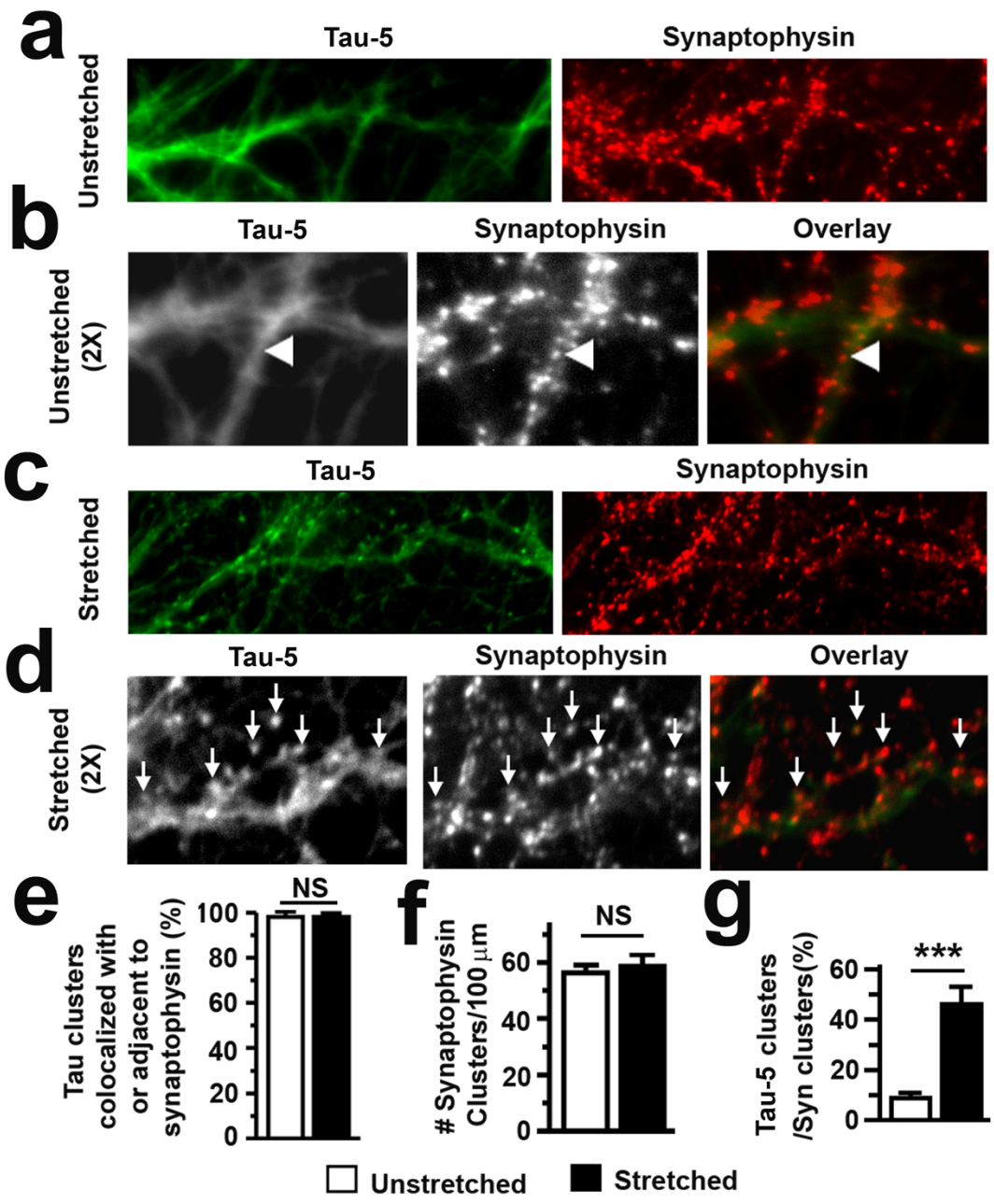

Figure 2.6 Endogenous tau forms distinct clusters that co-localizes with Synaptophysin following mechanical injury. (A) Unstretched neurons were co-stained for endogenous tau protein and pre-synaptic terminals using Tau-5 and anti-Synaptophysin antibodies, respectively. (B) 2X magnification of images from (A). Triangles denote

dendrites with diffusely stained tau but covered by distinct Synaptophysin clusters. (C) and (D) Similar images as in (A) and (B) from stretched neurons. Arrows denote that endogenous tau were aggregated to form distinct clusters along dendrites after mechanical injuries. These tau clusters are colocalized with or attached to Synaptophysin clusters. (E) Over 98% of tau clusters are colocalized with or attached to Synaptophysin clusters (mean +/- stdev). It suggests that they are likely to be functional dendritic spines. (F) Quantification of Synaptophysin cluster density along unstretched and stretched neurites. (mean +/- stdev). (G) Quantification of the percentage of Synaptophysin clusters that colocalized with/attached to tau clusters over total number of Synaptophysin clusters (mean +/- stdev).

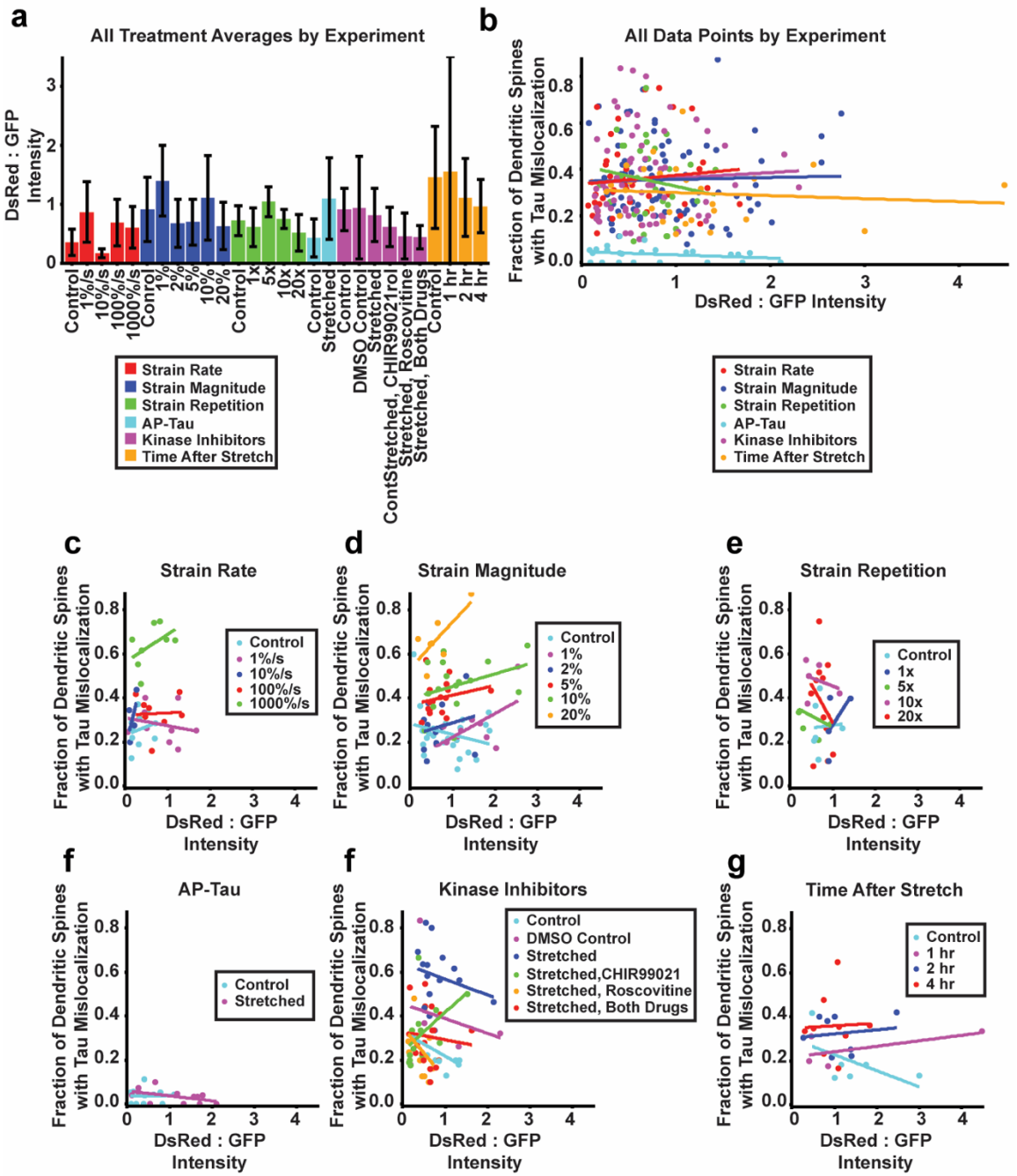

Figure 2.7 Quantification of DsRed and GFP relative intensities shows no correlation between fluorescence intensity ratio and observed tau mislocalization. (A) Ratio of DsRed:GFP (WT-Tau-GFP or APtau-GFP) intensity measured in each experimental treatment. Bar colors are grouped by experiment (higher ratio indicates increasing intensity of DsRed relative to GFP). (mean +/- stdev). (B) Scatterplot of observed tau mislocalization

vs. ratio of DsRed:GFP for each image acquired. Points and linear regression line colors are grouped by experiment. (C-G) Scatterplots of observed tau mislocalization vs. ratio of DsRed:GFP faceted by experiment. Within each plot, the points and linear regression line colors are grouped by experimental treatment.

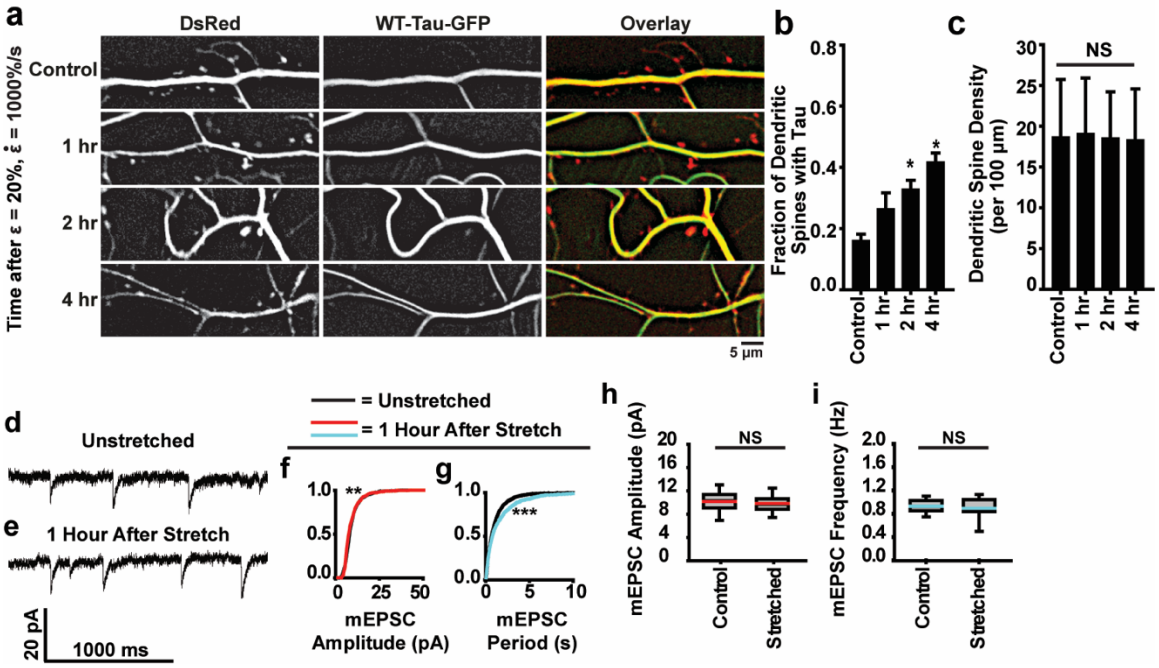

Figure 2.8 Tau mislocalization precedes synaptic deficits following a stretch-injury in neurons. (A) Representative images of tau mislocalization in neurons stretched to ε = 20% strain at varying times after injury (1, 2, and 4 hours). (B) Tau mislocalization, measured as fraction of spines with tau present, as an effect of time after stretch-injury. (spines/images): Control = 241/9, 1 hr = 165/6, 2 hr = 203/17, 4 hr = 232/10. (C) Total spine density as an effect of time after a stretch-injury. (D-E) Representative mEPSC recordings from unstretched neurons or neurons 1 hour after stretch-injury. (F) Cumulative frequency of mEPSC amplitudes (black: unstretched control, red: 1 hour after stretch, bins = 1 pA). (G) Cumulative frequency of mEPSC peak-to-peak period (black: unstretched

control, teal: 1 hour after stretch, bins = 50 ms). (H) Quantification of mEPSC amplitudes (black line: median, red: mean, box: 25%-75%, whisker: 10%-90%) (I) mEPSC frequency (black line: median, teal: mean, box: 25%-75%, whisker: 10%-90%)). For cumulative frequency distribution plots, K-S tests were used to compare treated and/or stretched groups to unstretched-untreated controls. D/D_{crit}: (f) 1.58, (g) 1.65, $\alpha = 0.05$ for all. (cells/mEPSCs): Unstretched = 14/1202, 1 Hour After Stretch = 12/1142. All plots: * denotes $P<0.05$, *** denotes $P < 0.001$ compared to control, *NS* is not significant. *Note:* K-S test significance is a highly sensitive non-parametric method that is possibly detecting some residual effects of TBI in (F-G) even though there is not a significant difference in the means of mEPSC amplitude or frequency, as seen in (H-I).

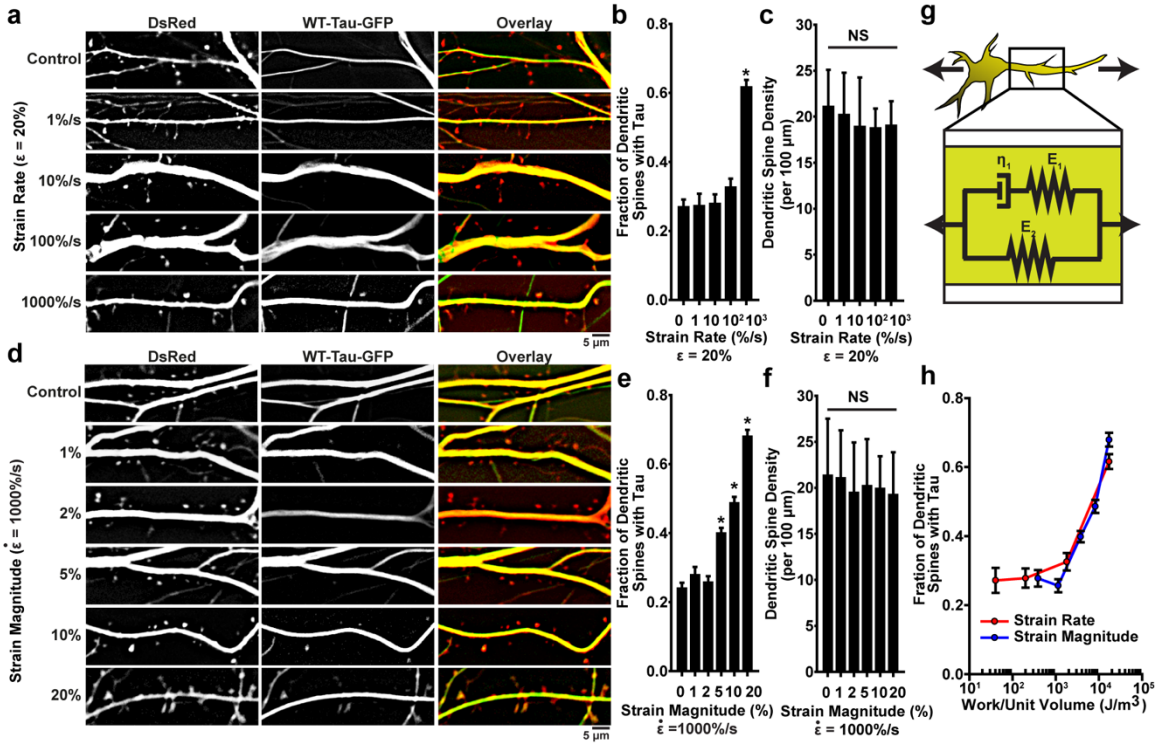

Figure 2.9 Tau mislocalization driven by mechanical injury is dependent on injury dynamics. (A) Representative images of tau mislocalization in neurons stretched to ε =

20% strain with varying strain rates ($\dot{\varepsilon}$ = 1, 10, 100, 1000%/s). (B) Tau mislocalization, measured as fraction of spines with tau present, as an effect of strain rate. (spines/images): Control = 402/10, 1%/s = 351/10, 10%/s = 259/7, 100%/s = 344/9, 1000%/s = 505/8. (C) Total spine density as an effect of strain rate. (D) Representative tau mislocalization in neurons stretched with varying strains (ε = 1, 2, 5, 10, 20%) at a strain rate of $\dot{\varepsilon}$ = 1000%/s. (E) Tau mislocalization, measured as fraction of spines with tau present, as an effect of strain magnitude. (spines/images): Control = 669/23, 1% = 346/10, 2% = 527/11, 5% = 866/16, 10% = 702/16, 20% = 542/7. (F) Spine density as an effect of strain magnitude. (G) Schematic representation of the standard viscoelastic solid used to model neurons during stretch. (H) Model-predicted mechanical work during stretching compared with experimentally measured tau mislocalization for all conditions measured in (A-F). (red: varying strain rate (A-C), blue: varying strain magnitude (D-F)). All plots: * denotes P<0.05 compared to control, *NS* is not significant.

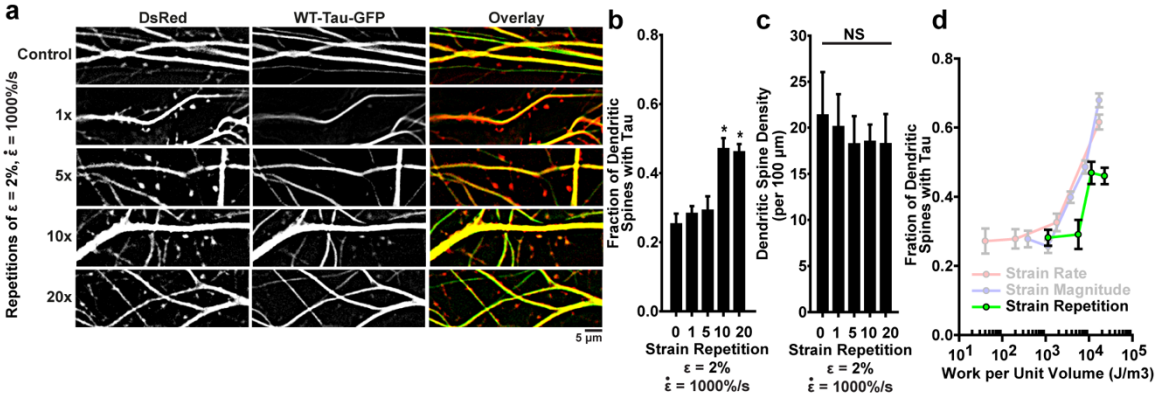

Figure 2.10 Repeated mild injuries induce tau mislocalization similar to a single severe injury. (A) Representative images of tau mislocalization in neurons exposed to periodic stretches of ε = 2%, $\dot{\varepsilon}$ = 1000%/s. (B) Tau mislocalization, measured as fraction

of spines with tau present, as an effect of number of stretches. (spines/images): Control = 299/9, 1x = 384/6, 5x = 277/6, 10x = 241/5, 20x = 437/5. (C) Spine density as an effect of number of stretches. (D) Additive work predicted by the viscoelastic model for repeated stretches compared with experimentally measured tau mislocalization. All plots: mean +/- stdev, * indicates P<0.05 compared to control, *NS* is not significant.

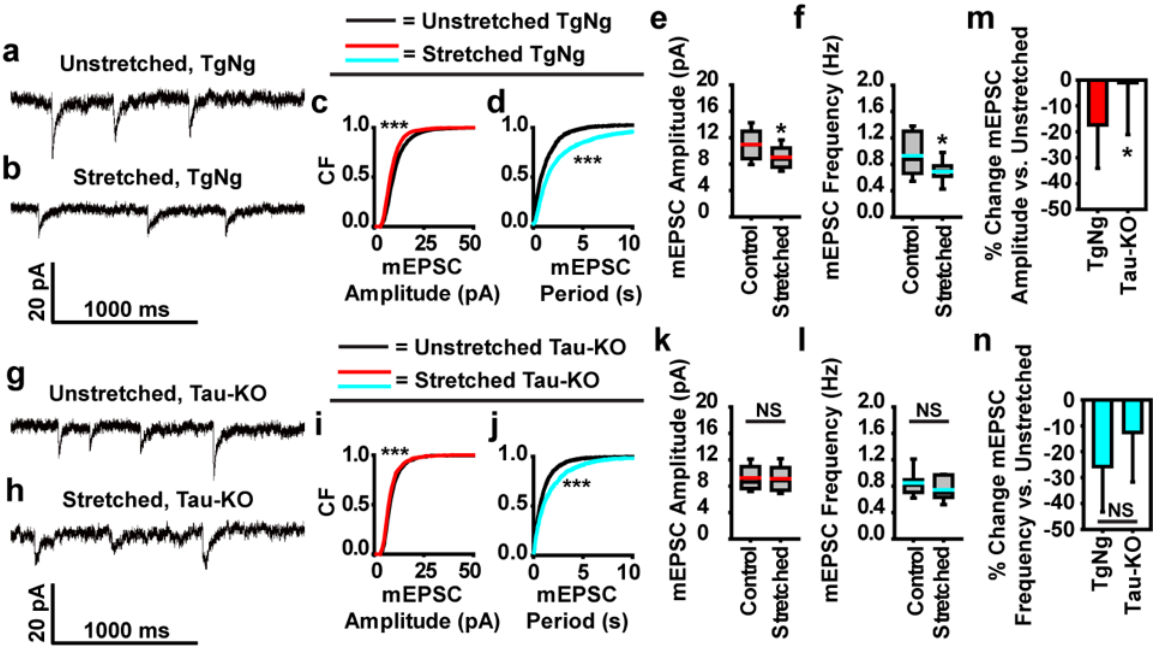

Figure 2.11 Blockage of postsynaptic dysfunction following stretch-injury and partial blockade of presynaptic dysfunction in tau knock-out mice. (A-B) Representative mEPSC recordings from TgNg neurons that were left unstretched or were injured with a stretch. (C) Cumulative frequency of mEPSC amplitudes (black: unstretched control, red: stretched, bins = 1 pA). (D) Cumulative frequency of mEPSC peak-to-peak period (black: unstretched control, teal: stretched, bins = 50 ms). (E) Quantification of mEPSC amplitudes (black line: median, red: mean, box: 25%-75%, whisker: 10%-90%) (f) mEPSC frequency (black line: median, teal: mean, box: 25%-75%, whisker: 10%-90%)). (G-H)

Representative mEPSC recordings from Tau-KO neurons that were left unstretched or were injured with a stretch. (I) Cumulative frequency of mEPSC amplitudes (black: unstretched control, red: stretched, bins = 1 pA). (J) Cumulative frequency of mEPSC peak-to-peak period (black: unstretched control, teal: stretched, bins = 50 ms). (K) Quantification of mEPSC amplitudes (black line: median, red: mean, box: 25%-75%, whisker: 10%-90%) (L) mEPSC frequency (black line: median, teal: mean, box: 25%-75%, whisker: 10%-90%)). (M) Percentage change in mEPSC amplitude of stretched TgNg neurons relative to unstretched TgNg neurons (*left bar*) is compared with that in stretched Tau-KO neurons relative to unstretched Tau-KO neurons (*right bar*). (N) Percentage change in mEPSC frequency of stretched TgNg neurons relative to unstretched TgNg neurons (*left bar*) is compared with that in stretched Tau-KO neurons relative to unstretched Tau-KO neurons (*right bar*). For cumulative frequency distribution plots, K-S tests were used to compare treated and/or stretched groups to unstretched-untreated controls. D/D_{crit}: (C) 4.15, (D) 5.74, (I) 1.37, (J) 1.70, $\alpha = 0.05$ for all. (cells/mEPSCs): TgNg-Unstretched = 14/3197, TgNg-Stretched = 16/2985, Tau-KO-Unstretched = 11/1150, Tau-KO-Stretched = 11/1007. All plots: * denotes $P<0.05$, *** denotes $P < 0.001$ compared to control, *NS* is not significant.

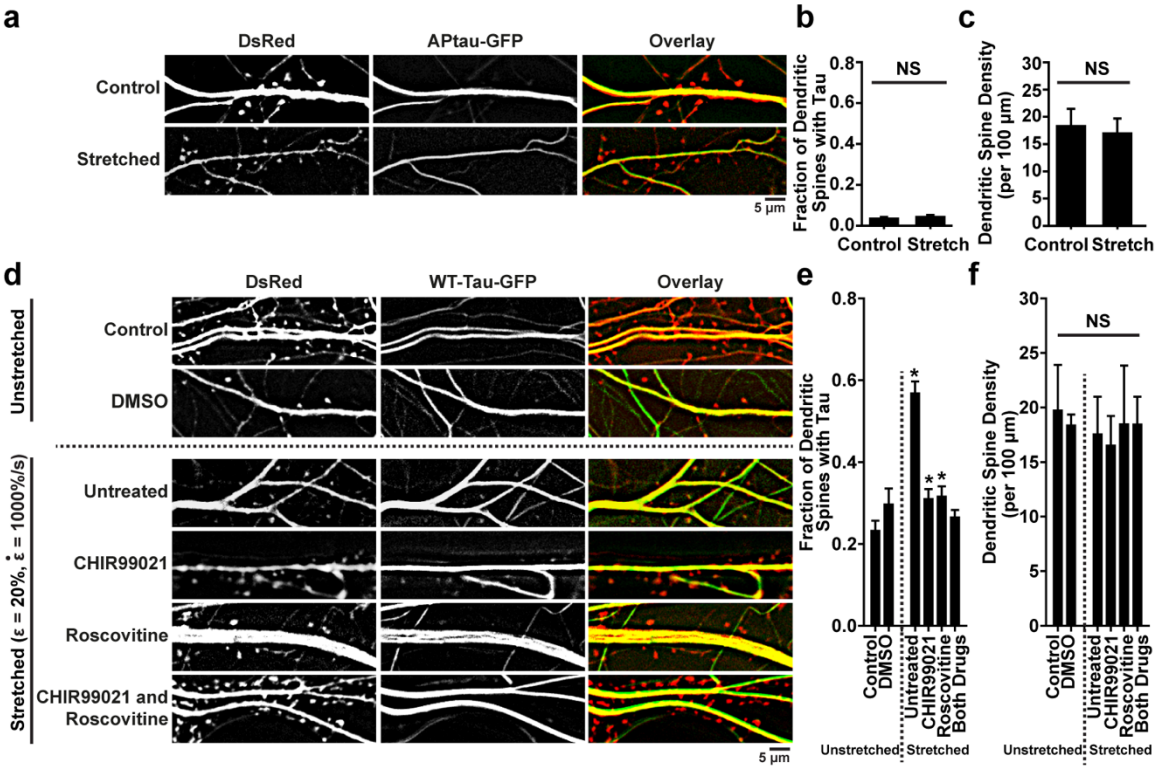

Figure 2.12 Tau mislocalization is phosphorylation-dependent. (A) Representative images of tau mislocalization in control and stretched (ε=20%,$\dot{\varepsilon}$=1000%/s) neurons transfected with DsRed and APtau-GFP, a form of tau that cannot be phosphorylated. (B) Quantification of tau mislocalization, measured as fraction of spines with tau present, in unstretched control and stretched neurons transfected with APtau-GFP. (spines/images): Control = 548/13, Stretched = 447/12. (C) Quantification of spine density in unstretched control and stretched neurons transfected with APtau-GFP. (D) Representative images of tau mislocalization in unstretched and stretched neurons (ε=20%,$\dot{\varepsilon}$=1000%/s) untreated, or treated with 500 nM CHIR99021 to inhibit GSK3β, 500 nM Roscovitine to inhibit CDK5, or both. (E) Tau mislocalization as an effect of stretch, following GSK3β and CDK5 inhibitor treatment. (spines/images): Control = 289/9, DMSO = 195/6, Untreated = 287/17, CHIR99021 = 324/10, Roscovitine = 365/15, Both Drugs = 582/18. (F) Spine density as

an effect of stretch, following GSK3β and CDK5 inhibitor treatment. All plots: mean +/- stdev, * indicates P<0.05, compared to unstretched control, *NS* is not significant.

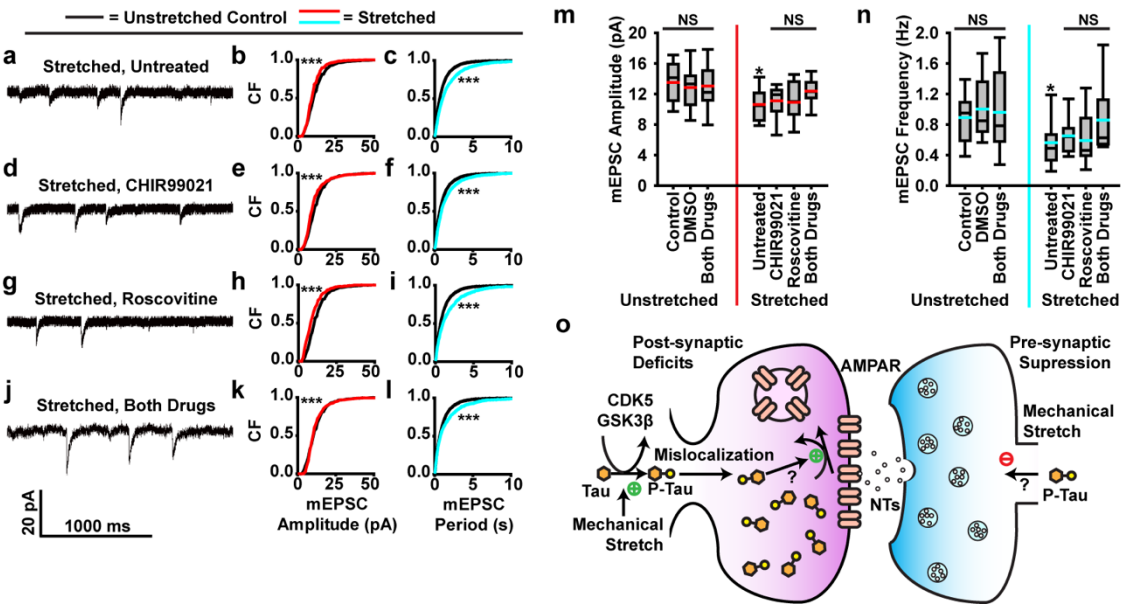

Figure 2.13 Stretch-induced tau mislocalization and hyperphosphorylation mediate synaptic dysfunction. (A-L) Effect of GSK3β and CDK5 inhibition on mEPSC dynamics. Left column: representative mEPSC recordings from neurons exposed to stretch. Center column: cumulative frequency of mEPSC amplitudes (black: unstretched control, red: stretched and treated, bins = 1 pA). Right column: cumulated frequency of mEPSC peak-to-peak period (black: untreated control, teal: stretched and treated, bins = 50 ms) (A-C) Untreated. (D-F) Pretreated with 500nM CHIR990021 to inhibit GSK3β. (G-I) Pretreated with 500 nM Roscovitine to inhibit CDK5. (J-L) Pretreated with both CHIR99021 and Roscovitine. (M) Quantification of mEPSC amplitudes (black line: median, red: mean, box: 25%-75%, whisker: 10%-90%) (N) mEPSC frequency (black line: median, teal: mean, box: 25%-75%, whisker: 10%-90%)) (O) Proposed molecular framework of the post-synaptic deficits and pre-synaptic suppression caused by mechanical injury. While

most postsynaptic deficits depend upon tau, other factors independent upon tau may contribute to presynaptic deficits. For cumulative frequency distribution plots, K-S tests were used to compare treated and/or stretched groups to unstretched-untreated controls. D/D_{crit}: (B) 4.31, (C) 5.48, (E) 4.79, (F) 3.33, (H) 5.11, (I) 4.30, (K) 1.82, (L) 2.98, α = 0.05 for all. (cells/mEPSCs): Control = 18/4360, DMSO = 13/1464, Unstretched-Both Drugs = 11/1571, Stretched-Untreated = 23/3139, CHIR99021 = 10/2481, Roscovitine = 11/1352, Stretched-Both Drugs = 14/1255. All plots: * denotes $P<0.05$, *** denotes $P < 0.001$ compared to control, *NS* is not significant. *Note*: K-S test significance in (K) is due to variations in low amplitude events, not a difference in the means (see M). Were these small events (< 7pA) excluded, the treated and control groups would not be significantly different. The two curves in (K) are obviously much closer than those in (B), (E) and (H), nevertheless, it is possible that the highly sensitive non-parametrical K-S test can still detect some residual effects of TBI.

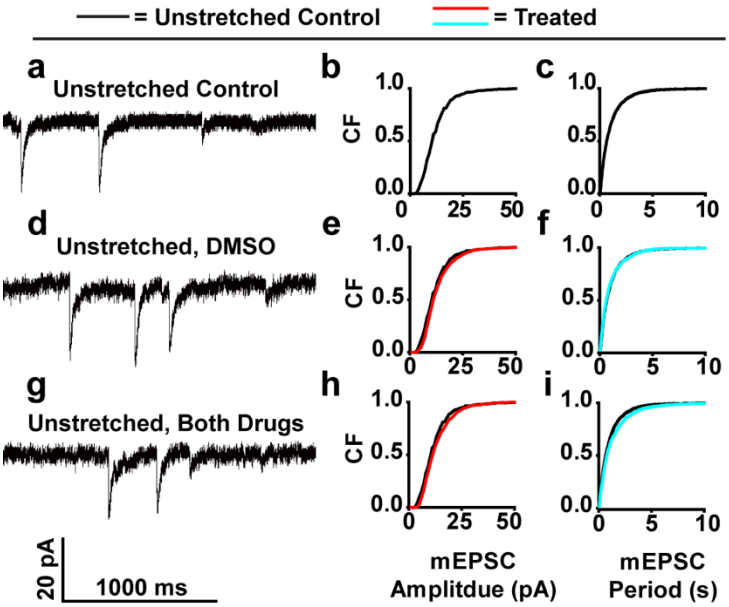

Figure 2.14 Synaptic function is not significantly influenced by DMSO, CHIR99021, or Roscovitine. (A-I) mEPSCs recorded from stretched neurons (left column), cumulative frequency distribution of mEPSC amplitudes of treated neurons compared to untreated neurons (center column, bins = 1 pA), and cumulative frequency distribution of mEPSC periods of treated neurons compared to untreated controls (right column, bins = 50 ms). For cumulative frequency distribution plots, K-S tests were used to compare treated and/or stretched groups to unstretched-untreated controls. In order: $D/D_{crit} = 2.24, 0.87, 2.42, 2.09$, $\alpha = 0.05$ for all. (spines/images): Unstretched-Control = (18/4360), Unstretched-DMSO = (13/1464), Unstretched-Both Drugs = (11/1571).

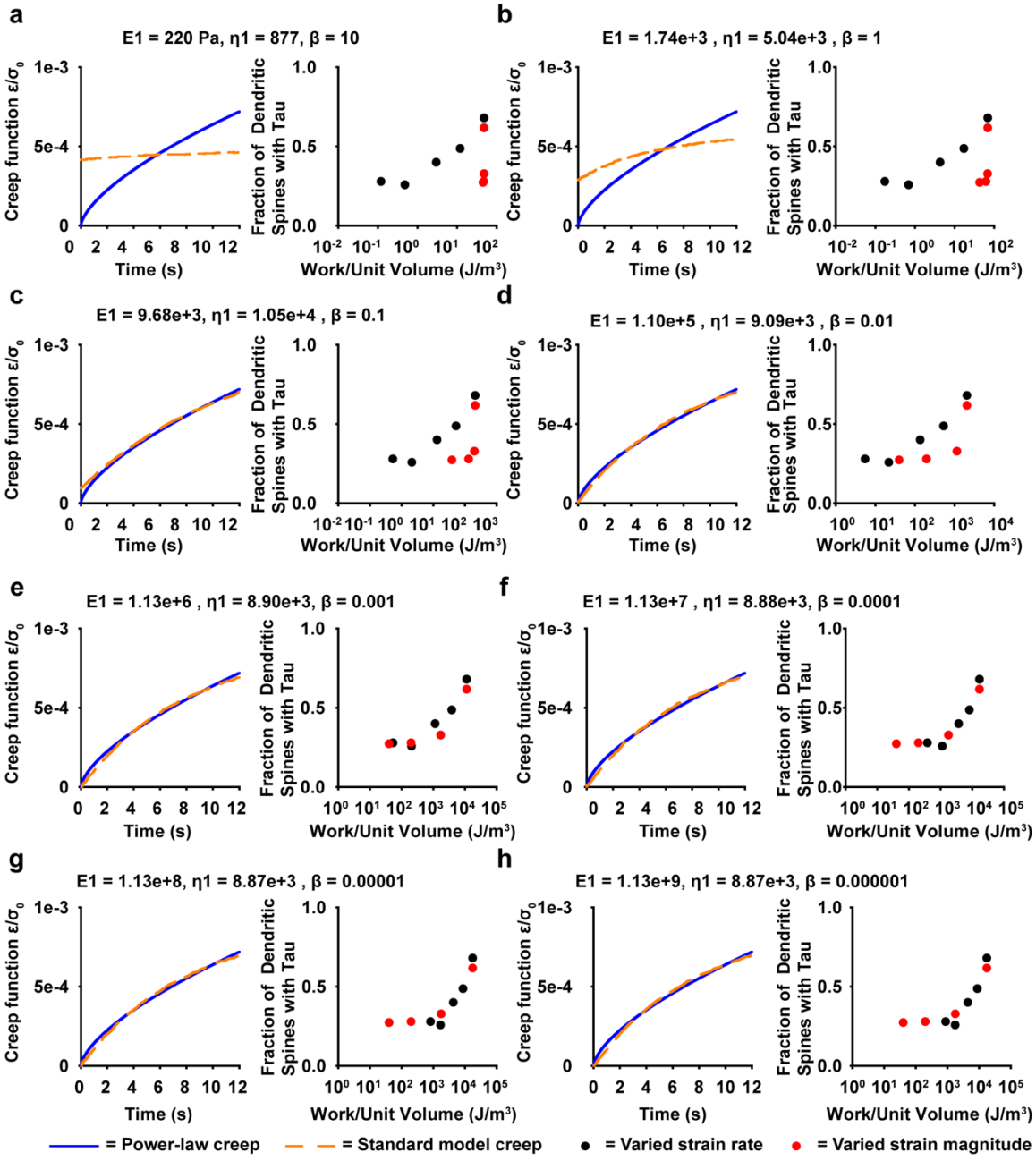

Figure 2.15 Parameter study of viscoelastic neuron model demonstrates that more fluidic material behavior better predicts the observed mislocalization data. Lu et al (2006) (90) modeled neurons as viscoelastic Kelvin solids. Grevesse et al (2015) (91) found that neurites are more fluidic than the soma. Here, we modeled the neuron as a standard viscoelastic solid (see Figure 2.9 G) and set $E_1 = \beta E_2$. As β increases, the material

behavior becomes more fluidic. For each set of plots: Left: Power-law description of measured creep behavior by Grevesse et al (blue solid line) vs the best standard model fit with the prescribed β (orange dashed line). Right: Model-predicted work vs experimentally measured tau mislocalization (black: varied strain rate (see Figure 2.9 A-C), red: varied strain magnitude (see Figure 2.9 D-F). (a) $\beta = 10$ (b) $\beta = 1$ (c) $\beta = 0.1$, (d) $\beta = 10^{-2}$, (e) $\beta = 10^{-3}$, (f) $\beta = 10^{-4}$, (g) $\beta = 10^{-5}$, (h) $\beta = 10^{-6}$.

Chapter 3. Orientation of Neurites Influences Severity of Mechanically-Induced Tau Pathology

This chapter contains currently unpublished material submitted for publication to Biophysical Journal. Braun, N.J., D. Liao, and P.W. Alford. 2021. Orientation of Neurites Influences Severity of Mechanically-Induced Tau Pathology. *Biophysical Journal.* Submitted 20210201.

3.1 Summary

Chronic traumatic encephalopathy (CTE) is a neurodegenerative disease associated with repeated traumatic brain injury (TBI). CTE is a tauopathy, in which cognitive decline is accompanied by the accumulation of neurofibrillary tangles of the protein tau in patients' brains. We recently found that mechanical force alone can induce tau mislocalization to dendritic spines and loss of synaptic function in *in vitro* neuronal cultures with random cell organization. However, in the brain, neurons are highly aligned, so here we aimed to determine how neuronal organization influences early-stage tauopathy caused by mechanical injury. Using microfabricated cell culture constructs to control the growth of neurites and an *in vitro* simulated-TBI device to apply controlled mechanical deformation, we found that neuronal orientation with respect to the direction of a uniaxial high-strain rate stretch injury influences the degree of tau pathology in injured neurons. We found that a mechanical stretch applied parallel to the neurite alignment induces greater mislocalization of tau proteins to dendritic spines than does a stretch with the same strain applied perpendicular to the neurites. Synaptic function, characterized by the amplitude of

miniature excitatory post-synaptic currents, was similarly decreased in neurons with neurites aligned parallel to stretch, while in neurons aligned perpendicular to stretch had little to no functional loss. Experimental injury parameters (strain, strain rate, direction of stretch) were combined with a standard viscoelastic solid model to show that, in our *in vitro* model, neurite work density during stretch correlates with tau mislocalization. These findings suggest that, in a TBI, the magnitude of brain deformation is not wholly predictive of neurodegenerative consequences of TBI, but that deformation relative to local neuronal architecture and the neurite mechanical energy during injury are better metrics for predicting trauma-induced tauopathy.

3.2 Introduction

Traumatic brain injury (TBI) is a serious public health concern due to its association with long-term neurological degeneration and cognitive decline (112, 113). TBIs are typically caused by falls, automobile crashes, sports-related impacts, and military-related injuries. Recent epidemiological studies in the United States indicate that there are approximately 2.8 million TBI-related emergency department visits, hospitalizations, and deaths per year. Additionally, an estimated 5.3 million Americans are living with a disability that stems from a TBI (2, 4, 114). However, these statistics likely underestimate the true impact of TBI, as mild TBIs frequently go unreported, especially in instances of violence (115, 116). Much of the current attention being paid to TBIs is due to the observation of long-term neurological deficits in those who have sustained multiple TBIs in their lives (notably in former professional athletes and military veterans), associated with chronic traumatic encephalopathy (CTE). CTE is a neurodegenerative disease whose

clinical symptoms include behavioral changes, memory deficits, and other symptoms of cognitive decline (5–9). CTE is one of several neurodegenerative diseases characterized by the dysfunction of the tau protein in neurons, called tauopathies, and is currently only confirmable via autopsy diagnosis.

Tau is a microtubule-associated protein that normally acts to stabilize microtubules and is involved in axonal transport in central nervous system neurons (67–69). Dense clusters of hyperphosphorylated tau, called neurofibrillary tangles (NFTs), are used to diagnose CTE and other tauopathies (75, 76). In CTE, the NFTs tend to be most concentrated in the brain's sulcal depths and in perivascular regions immediately surrounding blood vessels (8, 9, 15, 26, 76, 78). Computational models of TBI have shown that the strain experienced by these regions of the brain is amplified due to the geometry of the sulcus and the relative rigidity of blood vessels compared to brain tissue (66, 79). Studies of mechanical injury to axons suggest that strain is a primary determinant of neuronal damage and that different regions of the brain are disparately affected by strain (117–120). *In vitro* models of tauopathy (48, 49, 51, 72, 108) and TBI (66) have shown that tau becomes hyperphosphorylated and mislocalizes from axons to dendritic spines, where tau is not normally found. This mislocalization of tau leads to post-synaptic deficits due in part to AMPA-receptor internalization in the afflicted dendritic spine (48, 49, 51, 66, 72, 108). We have previously shown that cell-scale tau pathology and synaptic deficits can be elicited by a high-strain rate mechanical injury (66).

In situ, neurons are highly organized into various grey- and white-matter tracts. *In vivo* imaging of human brains during non-injurious head impacts have shown that distinct strain patterns emerge during impact that are dependent on these anisotropic architectural

differences (121). Computational models of axonal injury have yielded similar results, concluding that strain in the direction of neuronal orientation is one of the most significant predictors of traumatic or diffuse axonal injury (122, 123), and that inclusion of neuronal tract architecture improves finite-element models of brain deformation (124–128). In vitro studies have further shown that nerve bundle geometry affects neuron functionality after mechanical trauma (61, 129, 130). Taken together, these data suggest that the relative orientation of neuronal alignment and brain deformation during injury is an important mediator of injury outcome.

Here, using cultured hippocampal rat neurons, we report an *in vitro* tauopathy model of TBI that relates neuronal architecture and high-strain rate mechanical deformations to tau pathology and functional synaptic deficits. We find that neurons whose neurites are aligned parallel to stretch orientation showed significantly greater tau mislocalization than those aligned perpendicular to stretch or with no alignment when exposed to high strain rate strains. Loss of neuronal function, identified by miniature excitatory post-synaptic current (mEPSC) characteristics, was similarly greater in parallel aligned neurons. By combining TBI-simulation injury parameters (strain, strain rate, direction) with a standard viscoelastic solid material model and an image-based quantification of neuronal orientation, we calculated the work density during TBI-like stretching and found that total work density correlates with tau mislocalization, suggesting that tau mislocalization is mediated by mechanical energy during stretch. Taken together, these studies are an important step toward understanding the role of mechanical forces in tauopathy and the early stages of CTE.

3.3 Results

3.3.1 Substrate patterning influences neurite architecture *in vitro*

We previously developed an *in vitro* device to impart strains onto rat primary hippocampal neurons cultured on elastic membranes (Figure 3.1 A-B) (66). In our prior studies, the cells formed a monolayer with no discernable organization (Figure 3.2 A). Here, we aimed to direct neuronal organization to better mimic in vivo neural tracts by micropatterning ridges into PDMS-coated elastic membranes (Figure 3.2 B). Neurites of neurons seeded on the ridged substrates primarily aligned parallel to the ridges, resulting in cellular architecture that was distinct from neurons seeded on non-patterned substrates (Figure 3.2 C-E).

3.3.2 Neuronal alignment *in vitro* influences tau pathology caused by high strain-rate stretching

To investigate the effect of neuronal architecture on tau pathology, we used our custom-designed cell stretcher to simulate a TBI, *in vitro*, by applying high strain rate deformations to primary hippocampal neurons. Neurons were patterned so that neurites aligned parallel to or perpendicular to stretch, or they were left unpatterned so that neurite alignment was random (Figure 3.2 E). We co-transfected neurons with DsRed and WT-Tau-GFP plasmids to track the localization of tau within the neuron following a mechanical injury, allowing observation of tau mislocalization to dendritic spines (Figure 3.3 A-B). Neurons were exposed to a single stretch with a strain rate ($\dot{\varepsilon}$) of 1000%/s at a magnitude of 5%, 10%, or 20% strain (ε). Unstretched neurons showed a minimal amount of mislocalization in both patterned and unpatterned cells (Figure 3.4 A). Consistent with our

previous results, neurons with no preferred alignment showed increased tau mislocalization with increased strain magnitude. Neurons aligned parallel to stretch showed a similar relationship between tau and stretch, but the overall levels of tau mislocalization were higher for each prescribed injury level. Conversely, neurons aligned perpendicular to the stretch showed low levels of tau mislocalization in the control, 5% strain, and 10% strain conditions, and only showed a substantial increase in mislocalization at 20% strain (albeit still lower than the unaligned and parallel neurons) (Figure 3.4 B-E). These data suggest that neuronal injury, as characterized by tau mislocalization, is dependent on cellular architecture and correlated with the magnitude of the strain along the long axis of the neurites.

3.3.3 Loss of synaptic function following high velocity stretch is dependent on neuron architecture

In vitro models of Alzheimer's disease (AD) (48, 49, 51, 72) and our previous *in vitro* model of TBI (66) showed that tau mislocalization in neurons, induced by either a familial AD mutation or mechanical injury, was associated with synaptic deficits. Thus, we aimed to assess the impact of neuronal architecture-associated differences in mislocalization on these synaptic impairments following simulated TBI. Using whole-cell patch clamp, we recorded mEPSCs, which can be used as a proxy for synaptic functionality and health (Figure 3.5 A). We applied an intermediate stretch ($\varepsilon = 10\%, \dot{\varepsilon} = 1000\%/s$), at which our tau mislocalization experiments showed differential degrees of tau pathology between alignment groups. Consistent with our previous results, twenty-four hours after injury, we observed a statistically significant decrease in mEPSC amplitude, indicative of

post-synaptic dysfunction, between unstretched-unaligned neurons and stretched-unaligned neurons. In aligned neurons, we observed a significant decrease in mEPSC amplitude between unstretched neurons and neurons stretched parallel to neurite alignment, but not in those stretched perpendicular to neurite alignment (Figure 3.5 B, D-F). mEPSC frequency, which is indicative of pre-synaptic function, was not significantly affected by stretch (Figure 3.5 C, D-F). These data suggest that architecture-dependent tau mislocalization results in architecture-dependent post-synaptic deficit following mechanical injury.

3.3.4 Tau mislocalization is associated with mechanical energy during stretching

In our previous study, we found that tau mislocalization is both strain magnitude and strain rate dependent (66). This finding is consistent with other studies showing that neurites exhibit viscoelastic behavior (87–89, 131, 132). We modeled the neurite as a standard 1-D viscoelastic solid oriented parallel to the primary alignment of the neurite and determined the work density done on all neurites during stretching (Figure 3.6 A-B). In this model, neurites aligned parallel to stretch underwent substantially higher work than those aligned perpendicular to stretch (Figure 3.6 C), so, as expected neurons patterned to align parallel to stretch underwent higher mean work than unpatterned and perpendicularly patterned neurons (Figure 3.6 D). When neurons from our previous study were included (all unpatterned, but stretched with differing strains and strain rates), a distinct relationship between neurite work density and tau mislocalization was observed (Figure 3.6 E). These data suggest that the tau mislocalization observed following stretch is mediated by the mechanical energy added to the neurons during deformation.

3.4 Discussion

During TBI, neural tissues undergo high strain rate deformation throughout the brain that causes damage to neurons and glia (53, 93, 94, 96, 133). Brain injuries are not uniform, however, due to the anisotropic nature of the brain at both the tissue and cellular scale (117, 121, 126). Neurons and brain tissue behave viscoelastically, and brain injury is a function of both strain and strain rate of the tissue (87–89, 131, 132). Computational models of brain deformation during TBI show that strains are greatest in the sulcal depths and perivasculature regions, where geometric qualities or material differences between brain and vascular tissue contribute to heightened strain, respectively (66, 79). These same regions of the brain exhibit heightened presence of NFTs in CTE patient autopsies, suggesting that mechanical strain is the primary driver of NFT accumulation in TBI. Notably, neurons in the sulcal depths (and the cortex as a whole) are highly aligned into columnar architectures that are arranged perpendicular to the cortical surface (35–37). Here, we demonstrated that this cellular architecture may play an important role in determining the degree of mechanically-induced tauopathy caused by TBI.

Cellular architecture plays an important role in a wide range of cellular functions, including migration (134), cytoskeletal force generation (135, 136), and action potential propagation (137). Here, by stretching aligned neurons cultured on elastic substrates, we quantified the degree to which cellular architecture affects the tauopathic and synaptic consequences of TBI. In our previous study (66), regardless of neurite orientation, tau mislocalization to dendritic spines was observed in neurons exposed to large ($\varepsilon = 20\%$) strains with large strain rates ($\dot{\varepsilon} = 1000\%/s$). Here, at lower strains ($\varepsilon = 10\%$), however, the degree of tauopathy was notably dependent on alignment of the neurites with stretch.

These data suggest that the consequences of head injury depend not only on magnitude of the blow, but on the orientation of the force.

Our studies re-affirmed and extended previous results indicating that tau mislocalization is associated with functional synaptic deficits in affected neurons. We have reported previously in models of AD (51), Parkinson's disease (138), frontotemporal dementia with parkinsonism-17 (49), and TBI (66), that tau mislocalization to dendritic spines is associated with postsynaptic deficits. Here, a similar effect was observed, as decreased mEPSC amplitudes coincided with higher levels of tau mislocalization, suggesting that mechanically-driven tau mislocalization decreases the number of AMPA receptors present on a dendritic spine (102, 108). mEPSC amplitude decreases were also apparent in neurons aligned parallel to stretch. But, in neurons aligned perpendicular to stretch, the decreases were not significant. Interestingly, unlike at high strain ($\varepsilon = 20\%$) which we have previously studied (66), mechanical stretching at a lower strain ($\varepsilon = 10\%$) caused minimal impairment in presynaptic function (mESPC frequency), suggesting that postsynaptic functions are more vulnerable to some consequences of mechanical stretching than presynaptic functions. We saw a uniform (non-significant) decrease in frequency in all groups exposed to stretch, which did not correlate with the non-uniform tau mislocalization.

The mechanisms by which mechanical injury leads to CTE are not well-understood. In healthy neurons, tau is located on axonal microtubules, but in chronic neurodegenerative tauopathies like AD, tau becomes hyperphosphorylated and mislocalizes to dendritic spines (48, 49, 51, 72, 108). Our results suggest that mechanical injury accelerates the mislocalization process, leaving the injured neurons phenotypically similar to those in

chronic tauopathies. Prior *in vitro* and *in silico* studies have shown that mechanical forces can induce microtubule rupture, resulting in neurite collapse, characterized by focal swelling (107, 120, 139, 140). While we did not observe focal swelling, our model suggests a similar mechanism, wherein cytoskeletal damage occurs when mechanical energy exceeds a threshold value, which results in tau release from microtubules. Further study is needed to better elucidate this pathway.

Finally, these results have potential clinically-translatable importance. A number of studies have been performed correlating the whole-head acceleration during impact with brain deformation and clinical outcomes (141–144). Our results suggest that neural architectures and mechanical energy added to a neuron during deformation are key factors mediating tauopathy after TBI at the cellular level. This cellular injury model, combined with comprehensive mapping of brain geometry and neuronal architecture within the brain, may prove useful as a component of an injury prediction model for victims of TBI in its various forms (145, 146). Understanding how the basic cellular subunits of the brain are affected by high-strain deformations is crucial in creating a biomechanical framework for computational TBI models and developing future clinical interventions.

3.5 Methods

3.5.1 Cell culture construct preparation

Standard photolithography techniques were used to created PDMS stamps patterned with a linear array of 5 μm raised features (147–150). 15 μm raised features were separated by 100 μm gaps, creating an array of linear channels. PDMS stamps were then placed into a vacuum desiccator with a petri dish that contained approximately 400 μL of

trichloro(1H,1H,2H,2H-perfluorooctyl)silane (Sigma-Aldrich, Saint Louis, MO) and left overnight to create a self-assembled monolayer of silane, which allows for easier release of the stamps from cured PDMS (151). The high-velocity stretching constructs were prepared for neuronal culture by first spin-coating a 10 μm thick layer of 1:1 Sylgard 527 PDMS (Ellsworth Adhesives, Germantown, WI) onto 2" x 3" rectangles of 0.010" thick silicone sheeting (SMI, Saginaw, MI). To emboss linear channels into membranes, the silanized PDMS stamps were delicately placed into the uncured PDMS layer and allowed to cure in an 80°C oven for at least two hours. After curing, the PDMS stamps were carefully removed and the membranes were suspended in tension between two custom-designed stainless-steel brackets (Oakdale Precision, Saint Paul, MN). A 1:10 Sylgard 184 PDMS (Ellsworth Adhesives, Germantown, WI) ring was then adhered to the membrane to contain culture media upon seeding of neurons. The assembled constructs were treated with a UVO-Cleaner (Jelight Co. Inc., Irvine, CA) for eight minutes and then incubated in a solution of 100 μg/mL poly-D-lysine and 4 μg/mL laminin (Sigma-Aldrich, Saint Louis, MO) overnight to promote cellular adhesion.

3.5.2 Cell isolation and culture

Primary hippocampal neurons were harvested from neonatal Hsd:Sprague Dawley rat pups as previously described (Envigo, Indianapolis, IN) (110). The hippocampal sections were isolated and pooled together into Earl's Balanced Medium with 1 mM D-glucose that was chilled on ice. Tissues were then digested and the resulting cells were seeded onto the stretching constructs at a density of approximately 10^6 cells per construct in plating media (minimal essential media with Earle's salts, 10 mM HEPES, 10 mM

sodium pyruvate, 0.5 mM glutamine, 12.5 μM glutamate, 10% FBS and 0.6% glucose) (Thermo Fisher Scientific, Walthan, MA). The day of harvest and plating was denoted as day-in-vitro 1 or DIV1. Four hours after plating, the media was replaced with fresh plating media to remove debris and non-adherent or dead cells. 24 hours after plating (DIV2), the media was replaced with NbActive1 neuron culture media (BrainBits LLC, Springfield, IL). Cells were kept in a 37°C, 5% CO_2 incubation environment for the duration of experiments. 50% of the media was removed and replaced with fresh NbActiv1 media on a weekly basis.

3.5.3 High-speed stretching of neurons

A linear motor (PS01-23x80F/100x160-HP-R, LinMot USA, Elkhorn, WI) was used to perform mechanical deformations of cultured hippocampal neurons seeded on our custom-designed cell culture constructs. The motor applied a high strain rate uniaxial injury to neurons by displacing one of the stretchable cell culture construct brackets. Finite control over strain (ϵ) and strain rate ($\dot{\epsilon}$) allowed us to perform a variety of injury simulations. Single stretches were performed with $\epsilon = 0\ to\ 20\%$ and $\dot{\epsilon} = 1000\ \%/s$. This setup was used to deform all neurons in the study, including neurons aligned parallel to the stretch, perpendicular to the stretch, and neurons that were unaligned.

3.5.4 Transfection constructs

The DsRed construct used was expressed in the pRK5 vector and driven by a cytomegalovirus (CMV) promoter. The human-tau construct used in this study was expressed in the pRK5 vector, tagged with enhanced GFP on the N-terminus, and driven

by a CMV promoter (Clontech, Inc., Mountain View, CA). This WT-Tau-GFP construct encoded for human 4R tau lacking the N-terminal sequences (4R0N) and contained exons 1, 4-5, 7, and 9-13, intron 13, and exon 14.

3.5.5 Transfection and cellular imaging

Neurons were transfected with DsRed and WT-Tau-GFP using a standard calcium phosphate transfection method at DIV7 (111). Neurons were transfected at a 2:1 ratio of DsRed to WT-Tau-GFP. DsRed was used to visualize the morphology of the neurons, including the dendritic spines, while WT-Tau-GFP was used to track the localization of tau within the neuron. Transfected cells were allowed to mature for three weeks before experimentation. On DIV30, 24 hours after a stretch was applied, the neuron-containing constructs were mounted on a custom-designed platform above a Nikon inverted epifluorescent microscope. Images were collected using a 40x water immersion objective lens. 15-image stacks with a 0.5-micron step in the z-direction were acquired using a computerized focus motor and MetaMorph Imaging System (Universal Imaging Corporation, Bedford Hills, NY). After acquisition, stacks were processed using MetaMorph's 2D nearest-neighbors deconvolution method before out-of-focus slices were removed. The remaining slices of the stack were then averaged into a single image. DsRed and WT-Tau-GFP imaged were overlaid and colorized using Adobe Photoshop (Adobe Inc, San Jose, CA) to count dendritic spines and dendritic spines that contained tau. Each spine was treated as a datapoint with a binary outcome (tau present or no tau present) and the total sample population of dendritic spines was used for statistical analysis.

3.5.6 Electrophysiology

Miniature excitatory post-synaptic currents (mEPSCs) were recorded from hippocampal neurons at DIV30 using 5 megaohm glass pipettes. Whole-cell recording was performed with a holding potential of -55 mV (49). Recordings lasted up to five minutes, and were done using an Axopatch 200B amplifier and pClamp 11 (Molecular Devices, San Jose, CA). For each second recorded, a sweep of 200 ms was sampled. Recordings were filtered at 1 kHz and the gain was set to $\alpha = 1$. Before recording, neurons were rinsed three times with artificial cerebrospinal fluid (ACSF) at room temperature. 2 mL of ACSF was left in each construct during recording. ACSF was comprised of 119 mM NaCl, 2.5 mM KCl, 5.0 mM CaCl2, 2.5 mM MgCl2, 26.2 mM NaHCO3, 1 mM NaH2PO4 and 11 mM glucose. Additionally, ACSF was supplemented with 100 μM APV (an NMDAR antagonist), 1 μM TTX (a sodium channel blocker), and 100 μM picrotoxin (GABAa receptor antagonist) and bubbled with 95% O_2-5% CO_2 for 20 minutes before experiments. The glass patch pipette was filled with an internal solution comprised of 100 mM cesium gluconate, 0.2 mM EGTA, 0.5 mM $MgCl_2$, 2 mM ATP, 0.3 mM GTP, and 40 mM HEPES (pH 7.2 with CsOH) (Sigma-Aldrich, Saint Louis, MO). Each individual mEPSC was manually identified using MiniAnalysis software (Synaptosoft Inc, Fort Lee, NJ) based on a threshold amplitude of 3 pA, a characteristic fast-rising phase, and a slow decaying phase indicative of mEPSCs. The average amplitude of mEPSCs and the overall frequency of mEPSCs for each neuron was calculated and treated as a single datapoint.

3.5.7 Viscoelastic model of neurite deformation

Mechanical energy added to the dendritic spine during injury was determined by calculating the work density (work per unit volume) done on the cell during stretching, as described in our previous manuscript (66). Local neurite orientation angle (θ) relative to stretch orientation throughout the neuron was determined using DsRed images of individual neurons and a custom MATLAB code (135, 136, 152, 153). The local strain (ϵ) parallel to neurite alignment was taken as a function of applied strain ($\epsilon_{applied}$), such that

$$\epsilon = \epsilon_{applied} \cos^2 \theta$$

Neurons act as viscoelastic Kelvin solids (90), but neurites become more fluidic with increasing stress (91). To capture both of these observations, we modeled the neurite as a standard viscoelastic solid with two springs and one dashpot and described by the equation

$$\frac{\dot{\sigma}}{E_1} + \frac{\sigma}{\eta_1} = \frac{E_1+E_2}{E_1}\dot{\epsilon} + \frac{E_2}{\eta_1}\epsilon \quad (2)$$

where σ is the stress, ϵ is the strain, $\dot{\sigma}$ and $\dot{\epsilon}$ are the stress and strain rates, respectively, E_1 and E_2 are the moduli of the springs and η_1 is the viscosity of the dashpot. E_1, E_2, and η_1 were determined by simulating a creep test previously reported by Grevesse et al (91), and fitting the parameters to their results using least squares fitting (66). This method yielded: $E_1 = 1.133 \times 10^7$, $E_2 = 1.133 \times 10^3$, and $\eta_1 = 8.876 \times 10^3$.

To model neurite stretching, we let ϵ and $\dot{\epsilon}$ match those applied experimentally and calculated σ using Eq (2) and finite differences. The work density (w) was taken as

$$w = \int \sigma \, d\epsilon \quad (3)$$

over the period from the initiation of stretch to the time at which ϵ is at its peak value. Whole-neuron mean work density is reported.

3.5.8 Statistical analyses

To quantify tau mislocalization, the total number of dendritic spines and the number of dendritic spines containing an observable tau presence were recorded (spines and spines with tau were summed from all recorded images in each treatment group). The fraction of dendritic spines containing tau was calculated from these two numbers. A Chi-squared test for multiple proportions was used to assess for statistical differences between treatment groups, followed by two-proportion pooled z-tests to determine pairwise statistically significant differences between each of the treatment groups. For electrophysiology data (mEPSC amplitude and frequency) and mean work density vs strain data, one-way ANOVA was used to test for variance between all groups, followed thereafter by a Tukey *post-hoc* test for pairwise comparisons. For cumulative frequency distributions, Kolmogorov–Smirnov (K-S) tests were used to compare mEPSC amplitude and period distributions between unstretched cells and stretched groups (unaligned, parallel, and perpendicular). The ratio of the K-S test statistic (D) to the statistical critical value (D_{crit}) is reported in the figure captions. All tests had statistical significance set for $\alpha = 0.05$. Chi-squared tests, two-proportion pooled z-tests, ANOVA, and Tukey tests were performed using SigmaPlot 11.0 (Systat Software Inc., San Jose, CA). K-S tests were performed using Microsoft Excel (Microsoft, Seattle, WA).

3.5.9 Animal usage

The breeding, handling and usage of rats and mice have been approved by the Intuitional Animal Care and Use Committee (IACUC) at the University of Minnesota

(Protocol #1809-36344A). Rat pups (< 1 week old) were decapitated to harvest brain tissues strictly following the IACUC guidelines.

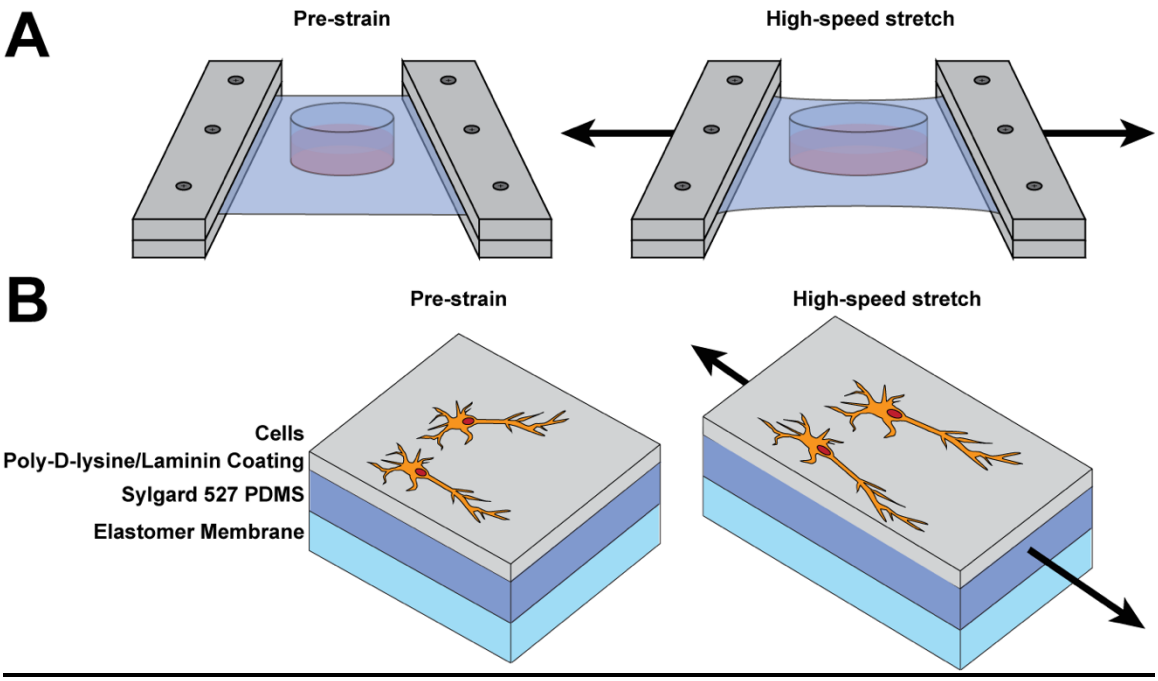

Figure 3.1: *In vitro* TBI simulations are performed on elastic cell culture constructs. (A) A neuron-containing elastic substrate was deformed at high speeds by a linear motor. (B) The elastic substrate upon which neurons were cultured was comprised of an elastic membrane layer spin-coated with Sylgard 527 PDMS and surface-coated with poly-D-lysine and laminin.

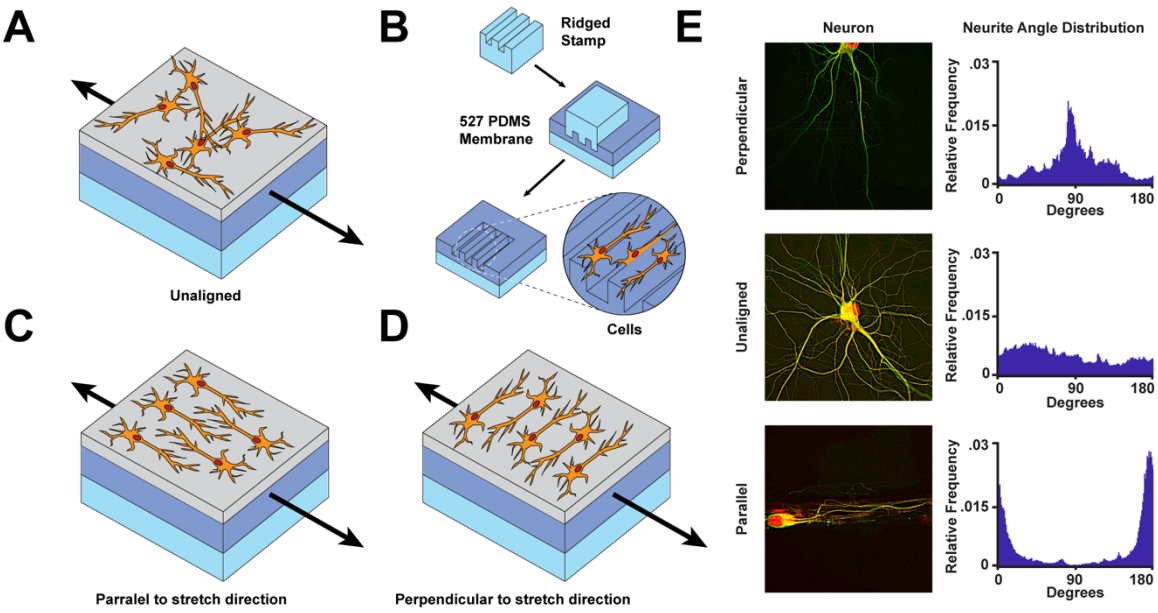

Figure 3.2: Embossing PDMS ridges onto cell culture constructs allows for preferential alignment of neuron growth along a chosen axis. (A) Without alignment, neurons form an unorganized monolayer on cell culture constructs. (B) Method for embossing ridges onto elastic membranes using a PDMS stamp. (C) Neurons aligned parallel to the axis of stretch. (D) Neurons aligned perpendicular to the axis of stretch. (E) Fluorescent images of neurons in the three alignment states (*left)* with accompanying neurite angle histograms (*right*), demonstrating the utility of this method.

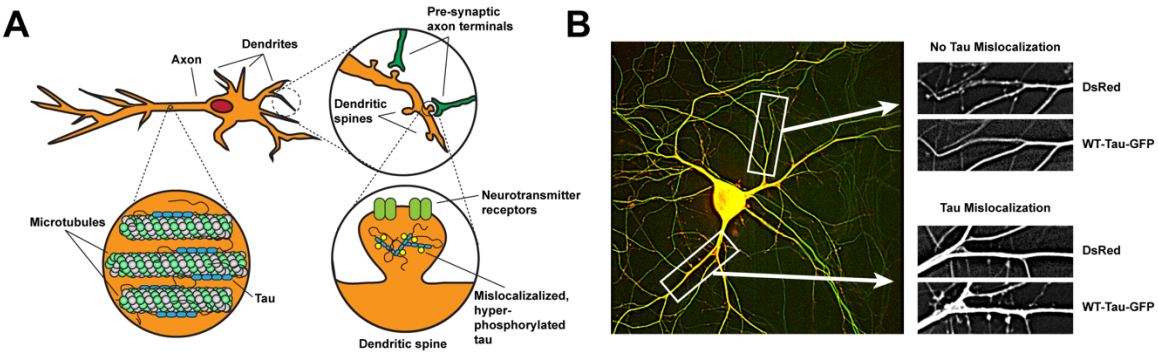

Figure 3.3: Tau mislocalizes to dendritic spines and ultimately aggregates into NFTs in tauopathies. (A) Post-synaptic neuron with tau bound to its axonal microtubules (*bottom left magnification*). Synapses with pre-synaptic neurons occur at the dendritic spines (*top right magnification*). Hyperphosphorylated tau that has mislocalized to and aggregated within a dendritic spine, where it interferes with AMPA receptor trafficking (*bottom right magnification*). (B) A representative neuron transfected to express DsRed and WT-Tau-GFP fluorescent proteins (*left*). A dendrite without significant tau mislocalization to dendritic spines (*top right*) and a dendrite with tau mislocalization to dendritic spines (*bottom right*).

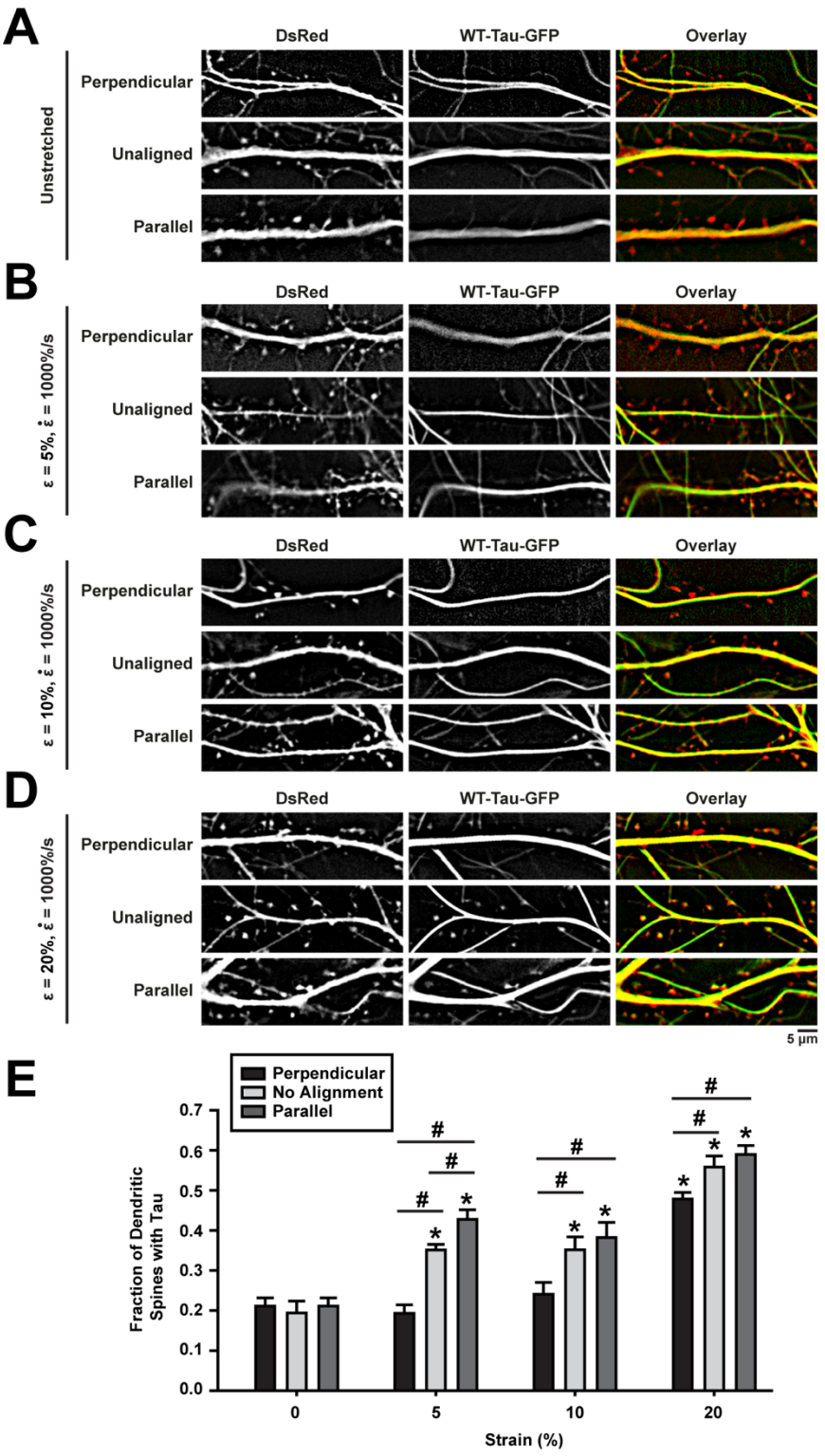

Figure 3.4: Tau mislocalization driven by mechanical injury is dependent on cellular architecture and injury severity. (A-D) Representative images of cultured rat

hippocampal neurons transfected with DsRed (left), WT-Tau-GFP (center). Images overlaid to assess tau mislocalization (right). Alignment configurations relative to the axis of stretch: perpendicular (top), unaligned (middle), parallel (bottom). (A) Unstretched neurons. (B) Neurons stretched to 5% strain at 1000%/s. (C) Neurons stretched to 10% strain at 1000%/s. (D) Neurons stretched to 20% strain at 1000%/s. (E) Quantification of tau mislocalization, measured as fraction of spines with tau present. (mean +/- stdev). (spines/images): 0-perpendicular = 412/10, 0-unaligned = 273/13, 0-parallel = 413/10, 5-perpendicular = 352/10, 5-unaligned = 1134/18 , 5-parallel = 428/12 , 10-perpendicular = 216/10 , 10-unaligned = 219/10, 10-parallel = 205/10, 20-perpendicular = 951/17, 20-unaligned = 319/11, 20-parallel = 507/16. # indicates statistical difference from other alignments within a strain group, * indicates statistical difference between unstretched cells in a given alignment, $P<0.05$. Note: 0-perpendicular and 0-parallel are the same data point, as cells are simply aligned without a stretch. Additionally, all images were cropped and rotated for efficiency. A perfect left-to-right stretch from the shown perspective only occurred in the parallel configurations of (B-D).

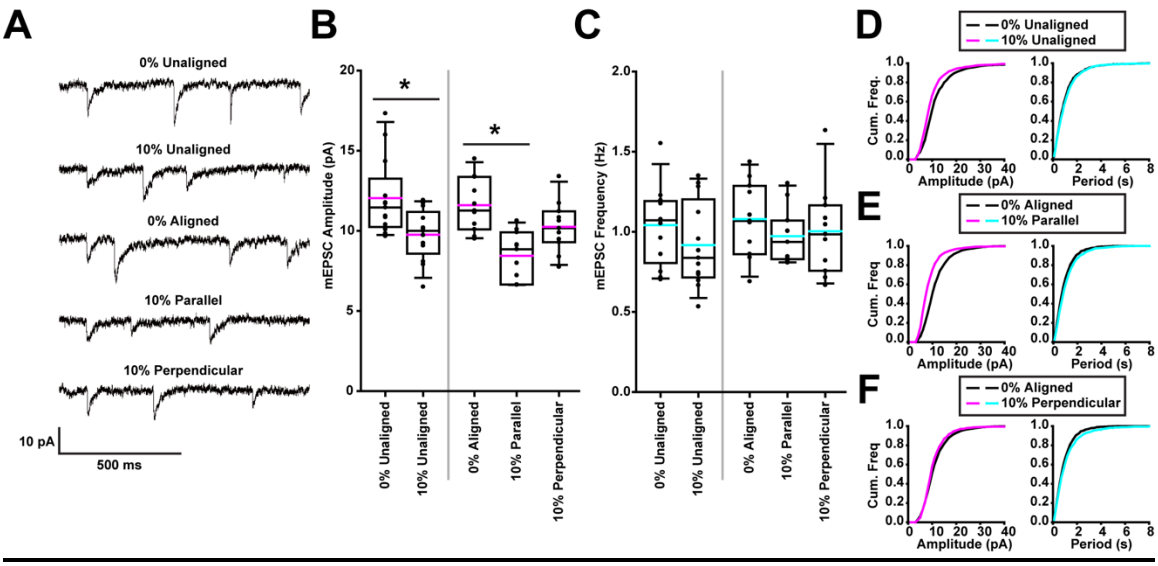

Figure 3.5: Neuron synaptic function after exposure to a stretch injury is dependent on architectural alignment. (A) Representative mEPSCs from each of the five stretch and alignment combinations (all stretches were 10% strain, 1000%/s). (B) Quantification of mEPSC amplitudes (black line: median, pink line: mean, box: 25%-75%, whisker: 10%-90%). (C) Quantification of mEPSC frequency (black line: median, blue: mean, box: 25%-75%, whisker: 10%-90%). (D) Cumulative frequency distribution of mEPSC amplitudes (*left*) and peak-to-peak periods (*right*) of unstretched-unaligned neurons vs stretched-unaligned neurons. (E) Cumulative frequency distribution of mEPSC amplitudes (*left*) and peak-to-peak periods (*right*) of unstretched-aligned neurons vs stretched-parallel neurons. (D) Cumulative frequency distribution of mEPSC amplitudes (*left*) and peak-to-peak periods (*right*) of unstretched-aligned neurons vs stretched-perpendicular neurons. (cells/mEPSCs): unstretched-unaligned = 13/2581, stretched-unaligned = 13/2231, unstretched-aligned = 11/2153, stretched-parallel = 11/1907, stretched-perpendicular = 11/1782. All plots: * denotes $P<0.05$.

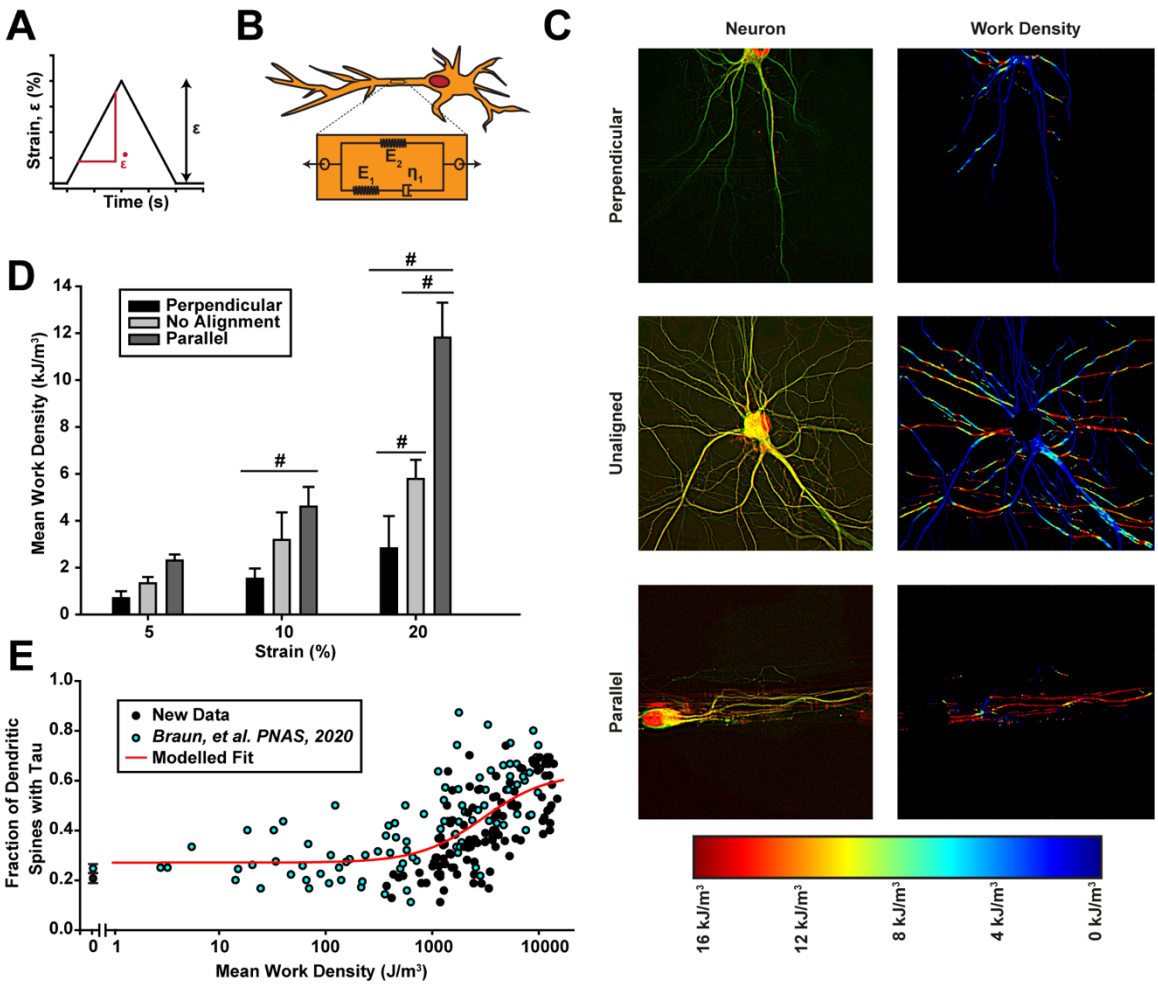

Figure 3.6: Viscoelastic model of stretched neurons demonstrates that mechanical work during injury causes tau mislocalization. (A) Example injury protocol for simulating TBI on neurons with strain (ε) and strain rate ($\dot{\varepsilon}$). (B) Standard linear solid model of viscoelasticity used to model neuron mechanical behavior. (C) Fluorescent images of neurons in the three alignment states (*left*) and heat maps showing work density done on the neuron from a ε = 20%, $\dot{\varepsilon}$ = 1000%/s stretch (*right*). (D) Quantification of mean work density, measured by averaging the mean work density of each imaged in an experimental group (mean +/- stdev). (images): 5-perpendicular = 10, 5-unaligned = 18, 5-parallel = 12, 10-perpendicular = 10, 10-unaligned = 10, 10-parallel = 10, 20-perpendicular = 17, 20-unaligned = 11, 20-parallel = 16. # indicates statistical difference from other

alignments within a strain group, $P<0.05$. (E) Experimentally-derived tau mislocalization vs mean work density done on a neuron during injury. *Black* points are new data from this study. *Blue* points are images from *Braun, et al. PNAS, 2020,* that were re-analyzed using this study's methods. The two points with a mean work density of zero represent the average (+/- stdev) tau mislocalization of all unstretched control neurons from both studies (n = 585 spines from this study, n = 1559 spines from *Braun, et al. PNAS, 2020*) (66). Modelled fit is based on a Hill equation (dose-response curve) and does not include the unstretched cells from each study (points with mean work density of zero). Note: cell somas were removed from images in (C) so that their rounded morphology would not affect calculations involving neurite architecture or alignment.

Chapter 4. Conclusion

4.1 Summary

The research described herein has led to three main conclusions: 1) the early pathological loci of NFTs in CTE brains are regions of high deformation during injury, 2) the mechanical energy associated with high strain rate deformation, relative to local neuronal architecture, can induce tau mislocalization to dendritic spines and synaptic deficits in cultured rat hippocampal neurons, and 3) these cellular changes are mediated through tau hyperphosphorylation and can be reversed through inhibition of GSK3β and CDK5 or genetic deletion of tau.

4.2 Impact

Soldiers and athletes exposed to frequent traumatic brain injuries have increased likelihood of developing a number of neurodegenerative diseases, including CTE. Through these works, we have characterized a portion of the neurocellular consequences of mechanical trauma and hypothesized how cell-scale dysfunction can manifest into tissue-scale disease and cognitive decline. By showing that tau mislocalization and some synaptic deficits can be mitigated by inhibiting hyperphosphorylation of tau by GSK3β and CDK5 kinases we have identified a potential therapeutic pathway that could be exploited to lessen some of the deleterious effects of TBI. Additionally, we have proposed a unique mechanistic model relating the amount of energy imparted on neurons to the tauopathic and synaptic consequences of TBI. This model may prove useful in predicting the neurodegenerative consequences of TBI based on the affected region of the brain and local

tissue and cellular architecture. As a whole, this work combines neuroscience and engineering techniques to improve our understanding of TBI and tauopathy.

4.3 Future directions

The work presented herein represents only the beginning stages of what could become a very productive investigation into TBI and CTE. Our methods could be improved greatly by increasing the experimental throughput to speed up analysis and allow for more experimental treatments at once. In terms of cell culture constructs, the current stretching constructs are rather large and only contain one chamber for cells to grow in. This results in a logistical problem of overcrowded cell-culture incubators and a limit to the number of treatments that can be studied during a given experimental run. This process could be improved by devising a multi-chambered stretching construct so that a variety of pharmaceuticals could be screened during a given experiment. Additionally, the image collection phase is currently done manually and is very time-consuming. By utilizing a microscope with an automated stage and/or computational cell detection capabilities, fluorescent images of transfected neurons could be acquired at a greater rate, allowing for more data collection. Constructing a TBI simulation device that mounts onto a microscope stage would also give the opportunity to capture the immediate cellular response to TBI, as opposed to the delayed measurement utilized in this work.

Finally, as with most *in vitro* work, it would be extremely valuable to replicate this work in an *in vivo* model. To this end, I constructed an *in vivo* TBI device for use on anesthetized rats that could be utilized in future research efforts. This device uses a similar linear motor as our *in vitro* stretcher that can be used to precisely and reproducibly induce

a mechanical deformation on a rat brain (after surgically drilling a small hole in the skull). Immunohistochemistry could then be used to assess the tauopathic or histological consequences of injury. Additionally, the electrophysiology experiments performed in this work could be recreated using brain slices from injured rats in an effort to validate previous *in vitro* results. Ultimately, the goal of this research is to improve the current state-of-knowledge on TBI and CTE, and the results outlined previously represent just the first steps on a long path.

References

1. Taylor, C.A., J.M. Bell, M.J. Breiding, and L. Xu. 2017. Traumatic Brain Injury–Related Emergency Department Visits, Hospitalizations, and Deaths — United States, 2007 and 2013. *MMWR. Surveill. Summ.* 66:1–16.
2. Roozenbeek, B., A.I.R. Maas, and D.K. Menon. 2013. Changing patterns in the epidemiology of traumatic brain injury. *Nat. Rev. Neurol.* 9:231–236.
3. Tagliaferri, F., C. Compagnone, M. Korsic, F. Servadei, and J. Kraus. 2006. A systematic review of brain injury epidemiology in Europe. *Acta Neurochir. (Wien).* 148:255–268.
4. Langlois, J.A., W. Rutland-Brown, and M.M. Wald. The epidemiology and impact of traumatic brain injury: a brief overview. *J. Head Trauma Rehabil.* 21:375–8.
5. Omalu, B.I., S.T. DeKosky, R.L. Minster, M.I. Kamboh, R.L. Hamilton, and C.H. Wecht. 2005. Chronic Traumatic Encephalopathy in a National Football League Player. *Neurosurgery*. 57:128–134.
6. Omalu, B.I., S.T. DeKosky, R.L. Hamilton, R.L. Minster, M.I. Kamboh, A.M. Shakir, and C.H. Wecht. 2006. Chronic Traumatic Encephalopathy In A National Football League Player: Part II. *Neurosurgery*. 59:1086–1093.
7. Omalu, B.I., J. Bailes, J.L. Hammers, and R.P. Fitzsimmons. 2010. Chronic Traumatic Encephalopathy, Suicides and Parasuicides in Professional American Athletes. *Am. J. Forensic Med. Pathol.* 31:130–132.
8. McKee, A.C., T.D. Stein, C.J. Nowinski, R.A. Stern, D.H. Daneshvar, V.E. Alvarez, H.-S. Lee, G. Hall, S.M. Wojtowicz, C.M. Baugh, D.O. Riley, C.A. Kubilus, K.A. Cormier, M.A. Jacobs, B.R. Martin, C.R. Abraham, T. Ikezu, R.R. Reichard, B.L.

Wolozin, A.E. Budson, L.E. Goldstein, N.W. Kowall, and R.C. Cantu. 2013. The spectrum of disease in chronic traumatic encephalopathy. *Brain*. 136:43–64.

9. Gavett, B.E., R.A. Stern, and A.C. McKee. 2011. Chronic Traumatic Encephalopathy: A Potential Late Effect of Sport-Related Concussive and Subconcussive Head Trauma. *Clin. Sports Med.* 30:179–188.

10. Armonda, R.A., R.S. Bell, A.H. Vo, G. Ling, T.J. DeGraba, B. Crandall, J. Ecklund, and W.W. Campbell. 2006. Wartime traumatic cerebral vasospasm: recent review of combat casualties. *Neurosurgery*. 59:1215–25; discussion 1225.

11. Goldstein, L.E., A.M. Fisher, C.A. Tagge, X.-L. Zhang, L. Velisek, J.A. Sullivan, C. Upreti, J.M. Kracht, M. Ericsson, M.W. Wojnarowicz, C.J. Goletiani, G.M. Maglakelidze, N. Casey, J.A. Moncaster, O. Minaeva, R.D. Moir, C.J. Nowinski, R.A. Stern, R.C. Cantu, J. Geiling, J.K. Blusztajn, B.L. Wolozin, T. Ikezu, T.D. Stein, A.E. Budson, N.W. Kowall, D. Chargin, A. Sharon, S. Saman, G.F. Hall, W.C. Moss, R.O. Cleveland, R.E. Tanzi, P.K. Stanton, and A.C. McKee. 2012. Chronic traumatic encephalopathy in blast-exposed military veterans and a blast neurotrauma mouse model. *Sci. Transl. Med.* 4:134ra60.

12. Bhattacharjee, Y. 2008. NEUROSCIENCE: Shell Shock Revisited: Solving the Puzzle of Blast Trauma. *Science (80-.).* 319:406–408.

13. Hoge, C.W., and C.A. Castro. Treatment of generalized war-related health concerns: placing TBI and PTSD in context. *JAMA*. 312:1685–6.

14. Hoge, C.W., D. McGurk, J.L. Thomas, A.L. Cox, C.C. Engel, and C.A. Castro. 2008. Mild Traumatic Brain Injury in U.S. Soldiers Returning from Iraq. *N. Engl. J. Med.* 358:453–463.

15. McKee, A.C., and M.E. Robinson. 2014. Military-related traumatic brain injury and neurodegeneration. *Alzheimers. Dement.* 10:S242-53.

16. Plassman, B.L., R.J. Havlik, D.C. Steffens, M.J. Helms, T.N. Newman, D. Drosdick, C. Phillips, B.A. Gau, K.A. Welsh-Bohmer, J.R. Burke, J.M. Guralnik, and J.C. Breitner. 2000. Documented head injury in early adulthood and risk of Alzheimer's disease and other dementias. *Neurology*. 55:1158–66.

17. Fleminger, S., D.L. Oliver, S. Lovestone, S. Rabe-Hesketh, and A. Giora. 2003. Head injury as a risk factor for Alzheimer's disease: the evidence 10 years on; a partial replication. *J. Neurol. Neurosurg. Psychiatry*. 74:857–62.

18. Bower, J.H., D.M. Maraganore, B.J. Peterson, S.K. McDonnell, J.E. Ahlskog, and W.A. Rocca. 2003. Head trauma preceding PD: a case-control study. *Neurology*. 60:1610–5.

19. Nemetz, P.N., C. Leibson, J.M. Naessens, M. Beard, E. Kokmen, J.F. Annegers, and L.T. Kurland. 1999. Traumatic brain injury and time to onset of Alzheimer's disease: a population-based study. *Am. J. Epidemiol.* 149:32–40.

20. Jawaid, A., R. Rademakers, J.S. Kass, Y. Kalkonde, and P.E. Schulz. 2009. Traumatic brain injury may increase the risk for frontotemporal dementia through reduced progranulin. *Neurodegener. Dis.* 6:219–20.

21. Gupta, R.K., and A. Przekwas. 2013. Mathematical Models of Blast-Induced TBI: Current Status, Challenges, and Prospects. *Front. Neurol.* 4:59.

22. Cullis, I.G. 2001. Blast waves and how they interact with structures. *J. R. Army Med. Corps*. 147:16–26.

23. Badachhape, A.A., R.J. Okamoto, R.S. Durham, B.D. Efron, S.J. Nadell, C.L.

Johnson, and P. V. Bayly. 2017. The Relationship of Three-Dimensional Human Skull Motion to Brain Tissue Deformation in Magnetic Resonance Elastography Studies. *J. Biomech. Eng.* 139:051002.

24. Xi, X., and P. Zhong. 2001. Dynamic photoelastic study of the transient stress field in solids during shock wave lithotripsy. *J. Acoust. Soc. Am.* 109:1226–39.

25. Covassin, T., R. Moran, and K. Wilhelm. 2013. Concussion Symptoms and Neurocognitive Performance of High School and College Athletes Who Incur Multiple Concussions. *Am. J. Sports Med.* 41:2885–2889.

26. McKee, A.C., R.C. Cantu, C.J. Nowinski, E.T. Hedley-Whyte, B.E. Gavett, A.E. Budson, V.E. Santini, H.-S. Lee, C.A. Kubilus, and R.A. Stern. 2009. Chronic traumatic encephalopathy in athletes: progressive tauopathy after repetitive head injury. *J. Neuropathol. Exp. Neurol.* 68:709–35.

27. Ito, K., Y. Asano, Y. Ikegame, and J. Shinoda. 2016. Differences in Brain Metabolic Impairment between Chronic Mild/Moderate TBI Patients with and without Visible Brain Lesions Based on MRI. *Biomed Res. Int.* 2016:1–8.

28. Gyoneva, S., and R.M. Ransohoff. 2015. Inflammatory reaction after traumatic brain injury: therapeutic potential of targeting cell–cell communication by chemokines. *Trends Pharmacol. Sci.* 36:471–480.

29. Koleske, A.J. 2013. Molecular mechanisms of dendrite stability. *Nat. Rev. Neurosci.* 14:536–550.

30. Lee, K.F.H., C. Soares, and J.-C. Béïque. 2012. Examining Form and Function of Dendritic Spines. *Neural Plast.* 2012:1–9.

31. Hering, H., and M. Sheng. 2001. DENDRITIC SPINES: STRUCTURE,

DYNAMICS AND REGULATION. *Nat. Rev. Neurosci.* 2:880–888.

32. Savier, E., S.J. Eglen, A. Bath?l?my, M. Perraut, F.W. Pfrieger, G. Lemke, and M. Reber. 2017. A molecular mechanism for the topographic alignment of convergent neural maps. *Elife*. 6.

33. Livet, J., T.A. Weissman, H. Kang, R.W. Draft, J. Lu, R.A. Bennis, J.R. Sanes, and J.W. Lichtman. 2007. Transgenic strategies for combinatorial expression of fluorescent proteins in the nervous system. *Nature*. 450:56–62.

34. Weissman, T.A., J.R. Sanes, J.W. Lichtman, and J. Livet. 2011. Generating and imaging multicolor Brainbow mice. *Cold Spring Harb. Protoc.* 2011:763–9.

35. Lodato, S., and P. Arlotta. 2015. Generating Neuronal Diversity in the Mammalian Cerebral Cortex. *Annu. Rev. Cell Dev. Biol.* 31:699–720.

36. da Costa, N.M., and K.A.C. Martin. 2010. Whose cortical column would that be? *Front. Neuroanat.* 4.

37. MOUNTCASTLE, V.B. 1957. Modality and topographic properties of single neurons of cat's somatic sensory cortex. *J. Neurophysiol.* 20:408–434.

38. Wang, Y., and E. Mandelkow. 2015. Tau in physiology and pathology. *Nat. Rev. Neurosci.* 17:22–35.

39. Mandelkow, E.-M., and E. Mandelkow. 2012. Biochemistry and Cell Biology of Tau Protein in Neurofibrillary Degeneration. *Cold Spring Harb. Perspect. Med.* 2:a006247–a006247.

40. Feinstein, S.C., and L. Wilson. 2005. Inability of tau to properly regulate neuronal microtubule dynamics: a loss-of-function mechanism by which tau might mediate neuronal cell death. *Biochim. Biophys. Acta - Mol. Basis Dis.* 1739:268–279.

41. Jayapalan, S., and J. Natarajan. 2013. The role of CDK5 and GSK3B kinases in hyperphosphorylation of microtubule associated protein tau (MAPT) in Alzheimer's disease. *Bioinformation*. 9:1023–30.

42. Martin, L., X. Latypova, C.M. Wilson, A. Magnaudeix, M.-L. Perrin, C. Yardin, and F. Terro. 2013. Tau protein kinases: Involvement in Alzheimer's disease. *Ageing Res. Rev.* 12:289–309.

43. Dolan, P.J., and G.V.W. Johnson. 2010. The role of tau kinases in Alzheimer's disease. *Curr. Opin. Drug Discov. Devel.* 13:595–603.

44. Hutton, M., J. Lewis, E. McGowan, J. Rockwood, H. Melrose, P. Nacharaju, M. Van Slegtenhorst, K. Gwinn-Hardy, M. Paul Murphy, M. Baker, X. Yu, K. Duff, J. Hardy, A. Corral, W.-L. Lin, S.-H. Yen, D.W. Dickson, and P. Davies. 2000. Neurofibrillary tangles, amyotrophy and progressive motor disturbance in mice expressing mutant (P301L) tau protein. *Nat. Genet.* 25:402–405.

45. Dorostkar, M.M., C. Zou, L. Blazquez-Llorca, and J. Herms. 2015. Analyzing dendritic spine pathology in Alzheimer's disease: problems and opportunities. *Acta Neuropathol.* 130:1–19.

46. Merino-Serrais, P., R. Benavides-Piccione, L. Blazquez-Llorca, A. Kastanauskaite, A. Rábano, J. Avila, and J. DeFelipe. 2013. The influence of phospho-τ on dendritic spines of cortical pyramidal neurons in patients with Alzheimer's disease. *Brain*. 136:1913–28.

47. Zempel, H., and E. Mandelkow. 2014. Lost after translation: missorting of Tau protein and consequences for Alzheimer disease. *Trends Neurosci.* 37:721–732.

48. Liao, D., E.C. Miller, and P.J. Teravskis. 2014. Tau acts as a mediator for

Alzheimer's disease-related synaptic deficits. *Eur. J. Neurosci.* 39:1202–13.

49. Hoover, B.R., M.N. Reed, J. Su, R.D. Penrod, L.A. Kotilinek, M.K. Grant, R. Pitstick, G.A. Carlson, L.M. Lanier, L.-L. Yuan, K.H. Ashe, and D. Liao. 2010. Tau mislocalization to dendritic spines mediates synaptic dysfunction independently of neurodegeneration. *Neuron*. 68:1067–81.

50. Anggono, V., and R.L. Huganir. 2012. Regulation of AMPA receptor trafficking and synaptic plasticity. *Curr. Opin. Neurobiol.* 22:461–9.

51. Miller, E.C., P.J. Teravskis, B.W. Dummer, X. Zhao, R.L. Huganir, and D. Liao. 2014. Tau phosphorylation and tau mislocalization mediate soluble Aβ oligomer-induced AMPA glutamate receptor signaling deficits. *Eur. J. Neurosci.* 39:1214–24.

52. Hemphill, M.A., S. Dauth, C.J. Yu, B.E. Dabiri, and K.K. Parker. 2015. Traumatic Brain Injury and the Neuronal Microenvironment: A Potential Role for Neuropathological Mechanotransduction. *Neuron*. 85:1177–1192.

53. Morrison, B., B.S. Elkin, J.-P. Dollé, and M.L. Yarmush. 2011. In Vitro Models of Traumatic Brain Injury. *Annu. Rev. Biomed. Eng.* 13:91–126.

54. Chen, Y.C., D.H. Smith, and D.F. Meaney. 2009. In-vitro approaches for studying blast-induced traumatic brain injury. *J. Neurotrauma*. 26:861–76.

55. Blank-Reid, C., and P.C. Reid. 2000. Penetrating trauma to the head. *Crit. Care Nurs. Clin. North Am.* 12:477–87.

56. Chuckowree, J.A., and J.C. Vickers. 2003. Cytoskeletal and morphological alterations underlying axonal sprouting after localized transection of cortical neuron axons in vitro. *J. Neurosci.* 23:3715–25.

57. MURPHY, E.J., and L.A. HORROCKS. 1993. A Model for Compression Trauma:

Pressure-Induced Injury in Cell Cultures. *J. Neurotrauma*. 10:431–444.

58. Shepard, S.R., J.B.G. Ghajar, R. Giannuzzi, S. Kupferman, and R.J. Hariri. 1991. Fluid percussion barotrauma chamber: A new in vitro model for traumatic brain injury. *J. Surg. Res.* 51:417–424.

59. LaPlaca, M.C., and L.E. Thibault. 1998. Dynamic mechanical deformation of neurons triggers an acute calcium response and cell injury involving theN-methyl-D-aspartate glutamate receptor. *J. Neurosci. Res.* 52:220–229.

60. SIEG, F., P. WAHLE, and H.-C. PAPE. 1999. Cellular Reactivity to Mechanical Axonal Injury in an Organotypic *in Vitro* Model of Neurotrauma. *J. Neurotrauma*. 16:1197–1213.

61. LaPlaca, M.C., D.K. Cullen, J.J. McLoughlin, and R.S. Cargill. 2005. High rate shear strain of three-dimensional neural cell cultures: a new in vitro traumatic brain injury model. *J. Biomech.* 38:1093–1105.

62. Cater, H.L., L.E. Sundstrom, and B. Morrison. 2006. Temporal development of hippocampal cell death is dependent on tissue strain but not strain rate. *J. Biomech.* 39:2810–2818.

63. Smith, D.H., J.A. Wolf, T.A. Lusardi, V.M. Lee, and D.F. Meaney. 1999. High tolerance and delayed elastic response of cultured axons to dynamic stretch injury. *J. Neurosci.* 19:4263–9.

64. Montenigro, P.H., C. Bernick, and R.C. Cantu. 2015. Clinical features of repetitive traumatic brain injury and chronic traumatic encephalopathy. *Brain Pathol.* 25:304–17.

65. Braak, H., D.R. Thal, E. Ghebremedhin, and K. Del Tredici. 2011. Stages of the

Pathologic Process in Alzheimer Disease: Age Categories From 1 to 100 Years. *J. Neuropathol. Exp. Neurol.* 70:960–969.

66. Braun, N.J., K.R. Yao, P.W. Alford, and D. Liao. 2020. Mechanical injuries of neurons induce tau mislocalization to dendritic spines and tau-dependent synaptic dysfunction. *Proc. Natl. Acad. Sci.* 202008306.

67. Chong, F.P., K.Y. Ng, R.Y. Koh, and S.M. Chye. 2018. Tau Proteins and Tauopathies in Alzheimer's Disease. *Cell. Mol. Neurobiol.* 38:965–980.

68. Conde, C., and A. Cáceres. 2009. Microtubule assembly, organization and dynamics in axons and dendrites. *Nat. Rev. Neurosci.* 10:319–332.

69. Chen, J., Y. Kanai, N.J. Cowan, and N. Hirokawa. 1992. Projection domains of MAP2 and tau determine spacings between microtubules in dendrites and axons. *Nature*. 360:674–677.

70. Kanaan, N.M., G.A. Morfini, N.E. LaPointe, G.F. Pigino, K.R. Patterson, Y. Song, A. Andreadis, Y. Fu, S.T. Brady, and L.I. Binder. 2011. Pathogenic forms of tau inhibit kinesin-dependent axonal transport through a mechanism involving activation of axonal phosphotransferases. *J. Neurosci.* 31:9858–68.

71. Zhou, L., J. McInnes, K. Wierda, M. Holt, A.G. Herrmann, R.J. Jackson, Y.-C. Wang, J. Swerts, J. Beyens, K. Miskiewicz, S. Vilain, I. Dewachter, D. Moechars, B. De Strooper, T.L. Spires-Jones, J. De Wit, and P. Verstreken. 2017. Tau association with synaptic vesicles causes presynaptic dysfunction. *Nat. Commun.* 8:15295.

72. Teravskis, P.J., B.R. Oxnard, E.C. Miller, L. Kemper, K.H. Ashe, and D. Liao. 2019. Phosphorylation in two discrete tau domains regulates a stepwise process leading to

postsynaptic dysfunction. *J. Physiol.* JP277459.

73. Le, M.N., W. Kim, S. Lee, A.C. McKee, and G.F. Hall. 2012. Multiple mechanisms of extracellular tau spreading in a non-transgenic tauopathy model. *Am. J. Neurodegener. Dis.* 1:316–33.

74. Armonda, R.A., R.S. Bell, A.H. Vo, G. Ling, T.J. DeGraba, B. Crandall, J. Ecklund, and W.W. Campbell. 2006. Wartime Traumatic Cerebral Vasospasm: Recent Review Of Combat Casualties. *Neurosurgery*. 59:1215–1225.

75. Lee, V.M.-Y., M. Goedert, and J.Q. Trojanowski. 2001. Neurodegenerative Tauopathies. *Annu. Rev. Neurosci.* 24:1121–1159.

76. McKee, A.C., T.D. Stein, P.T. Kiernan, and V.E. Alvarez. 2015. The neuropathology of chronic traumatic encephalopathy. *Brain Pathol.* 25:350–64.

77. Mckee, A.C., and D.H. Daneshvar. 2015. The neuropathology of traumatic brain injury. In: Handbook of clinical neurology. . pp. 45–66.

78. Montenigro, P.H., D.T. Corp, T.D. Stein, R.C. Cantu, and R.A. Stern. 2015. Chronic Traumatic Encephalopathy: Historical Origins and Current Perspective. *Annu. Rev. Clin. Psychol.* 11:309–330.

79. Ghajari, M., P.J. Hellyer, and D.J. Sharp. 2017. Computational modelling of traumatic brain injury predicts the location of chronic traumatic encephalopathy pathology. *Brain*. 140:333–343.

80. Hemphill, M.A., B.E. Dabiri, S. Gabriele, L. Kerscher, C. Franck, J.A. Goss, P.W. Alford, and K.K. Parker. 2011. A Possible Role for Integrin Signaling in Diffuse Axonal Injury. *PLoS One*. 6:e22899.

81. Alford, P.W., B.E. Dabiri, J.A. Goss, M.A. Hemphill, M.D. Brigham, and K.K.

Parker. 2011. Blast-induced phenotypic switching in cerebral vasospasm. *Proc. Natl. Acad. Sci.* 108:12705–12710.

82. Bayly, P. V., E.E. Black, R.C. Pedersen, E.P. Leister, and G.M. Genin. 2006. In vivo imaging of rapid deformation and strain in an animal model of traumatic brain injury. *J Biomech*. 39:1086–1095.

83. Purves, D., G. Augustine, D. Fitzpatrick, L. Katz, A. LaMantia, J. McNamara, and S. Williams. 2001. Neuroscience. In: Neuroscience. Sunderland (MA): Sinauer Associates.

84. Zhang, J., Y. Yang, H. Li, J. Cao, and L. Xu. 2005. Amplitude/frequency of spontaneous mEPSC correlates to the degree of long-term depression in the CA1 region of the hippocampal slice. *Brain Res.* 1050:110–117.

85. Lee, H.-K., K. Kameyama, R.L. Huganir, and M.F. Bear. 1998. NMDA Induces Long-Term Synaptic Depression and Dephosphorylation of the GluR1 Subunit of AMPA Receptors in Hippocampus. *Neuron*. 21:1151–1162.

86. Earnshaw, B.A., and P.C. Bressloff. 2006. Biophysical model of AMPA receptor trafficking and its regulation during long-term potentiation/long-term depression. *J. Neurosci.* 26:12362–73.

87. Feng, Y., E.H. Clayton, Y. Chang, R.J. Okamoto, and P. V Bayly. 2013. Viscoelastic properties of the ferret brain measured in vivo at multiple frequencies by magnetic resonance elastography. *J. Biomech.* 46:863–70.

88. Clayton, E.H., J.R. Garbow, and P. V Bayly. 2011. Frequency-dependent viscoelastic parameters of mouse brain tissue estimated by MR elastography. *Phys. Med. Biol.* 56:2391–2406.

89. Budday, S., G. Sommer, G.A. Holzapfel, P. Steinmann, and E. Kuhl. 2017. Viscoelastic parameter identification of human brain tissue. *J. Mech. Behav. Biomed. Mater.* 74:463–476.

90. Lu, Y.-B., K. Franze, G. Seifert, C. Steinhäuser, F. Kirchhoff, H. Wolburg, J. Guck, P. Janmey, E.-Q. Wei, J. Käs, and A. Reichenbach. 2006. Viscoelastic properties of individual glial cells and neurons in the CNS. *Proc. Natl. Acad. Sci. U. S. A.* 103:17759–64.

91. Grevesse, T., B.E. Dabiri, K.K. Parker, and S. Gabriele. 2015. Opposite rheological properties of neuronal microcompartments predict axonal vulnerability in brain injury. *Sci. Rep.* 5:9475.

92. McKee, A.C., T.D. Stein, P.T. Kiernan, and V.E. Alvarez. 2015. The Neuropathology of Chronic Traumatic Encephalopathy. *Brain Pathol.* 25:350–364.

93. Lucke-Wold, B.P., R.C. Turner, A.F. Logsdon, J.E. Bailes, J.D. Huber, and C.L. Rosen. 2014. Linking traumatic brain injury to chronic traumatic encephalopathy: identification of potential mechanisms leading to neurofibrillary tangle development. *J. Neurotrauma*. 31:1129–38.

94. Vogel, E.W., S.H. Rwema, D.F. Meaney, C.R. “Dale” Bass, and B. Morrison. 2017. Primary Blast Injury Depressed Hippocampal Long-Term Potentiation through Disruption of Synaptic Proteins. *J. Neurotrauma*. 34:1063–1073.

95. Brown, N.J., R.C. Mannix, M.J. O’Brien, D. Gostine, M.W. Collins, and W.P. Meehan. 2014. Effect of cognitive activity level on duration of post-concussion symptoms. *Pediatrics*. 133:e299-304.

96. Yang, J., C. Peek-Asa, T. Covassin, and J.C. Torner. 2015. Post-Concussion

Symptoms of Depression and Anxiety in Division I Collegiate Athletes. *Dev. Neuropsychol.* 40:18–23.

97. Meaney, D.F., B. Morrison, and C. Dale Bass. 2014. The mechanics of traumatic brain injury: a review of what we know and what we need to know for reducing its societal burden. *J. Biomech. Eng.* 136:021008.

98. Meythaler, J.M., J.D. Peduzzi, E. Eleftheriou, and T.A. Novack. 2001. Current concepts: Diffuse axonal injury–associated traumatic brain injury. *Arch. Phys. Med. Rehabil.* 82:1461–1471.

99. Ahmadzadeh, H., D.H. Smith, and V.B. Shenoy. 2014. Viscoelasticity of tau proteins leads to strain rate-dependent breaking of microtubules during axonal stretch injury: predictions from a mathematical model. *Biophys. J.* 106:1123–33.

100. Song, H., J. Cui, A. Simonyi, C.E. Johnson, G.K. Hubler, R.G. DePalma, and Z. Gu. 2018. Linking blast physics to biological outcomes in mild traumatic brain injury: Narrative review and preliminary report of an open-field blast model. *Behav. Brain Res.* 340:147–158.

101. Chen, Y., and S. Constantini. 2013. Caveats for using shock tube in blast-induced traumatic brain injury research. *Front. Neurol.* 4:117.

102. DEL CASTILLO, J., and B. KATZ. 1954. Quantal components of the end-plate potential. *J. Physiol.* 124:560–73.

103. Liao, D., N.A. Hessler, and R. Malinow. 1995. Activation of postsynaptically silent synapses during pairing-induced LTP in CA1 region of hippocampal slice. *Nature*. 375:400–404.

104. Abisambra, J.F., and S. Scheff. 2014. Brain Injury in the Context of Tauopathies. *J.*

Alzheimer's Dis. 40:495–518.

105. Okada, Y., H. Yamazaki, Y. Sekine-Aizawa, and N. Hirokawa. 1995. The neuron-specific kinesin superfamily protein KIF1A is a uniqye monomeric motor for anterograde axonal transport of synaptic vesicle precursors. *Cell*. 81:769–780.

106. Guedes-Dias, P., and E.L.F. Holzbaur. 2019. Axonal transport: Driving synaptic function. *Science (80-.).* 366:eaaw9997.

107. Tang-Schomer, M.D., V.E. Johnson, P.W. Baas, W. Stewart, and D.H. Smith. 2012. Partial interruption of axonal transport due to microtubule breakage accounts for the formation of periodic varicosities after traumatic axonal injury. *Exp. Neurol.* 233:364–372.

108. Teravskis, P.J., K.H. Ashe, and D. Liao. 2020. The Accumulation of Tau in Postsynaptic Structures: A Common Feature in Multiple Neurodegenerative Diseases? *Neuroscientist*. 26:503–520.

109. Budday, S., R. Nay, R. de Rooij, P. Steinmann, T. Wyrobek, T.C. Ovaert, and E. Kuhl. 2015. Mechanical properties of gray and white matter brain tissue by indentation. *J. Mech. Behav. Biomed. Mater.* 46:318–30.

110. Lin, H., R. Huganir, and D. Liao. 2004. Temporal dynamics of NMDA receptor-induced changes in spine morphology and AMPA receptor recruitment to spines. *Biochem. Biophys. Res. Commun.* 316:501–11.

111. Kingston, R.E., C.A. Chen, and J.K. Rose. 2003. Calcium Phosphate Transfection. *Curr. Protoc. Mol. Biol.* 63:9.1.1-9.1.11.

112. Moretti, L., I. Cristofori, S.M. Weaver, A. Chau, J.N. Portelli, and J. Grafman. 2012. Cognitive decline in older adults with a history of traumatic brain injury. *Lancet*

Neurol. 11:1103–1112.

113. Gardner, R.C., and K. Yaffe. 2015. Epidemiology of mild traumatic brain injury and neurodegenerative disease. *Mol. Cell. Neurosci.* 66:75–80.

114. Taylor, C.A., J.M. Bell, M.J. Breiding, and L. Xu. 2017. Traumatic brain injury-related emergency department visits, hospitalizations, and deaths - United States, 2007 and 2013. *MMWR Surveill. Summ.* 66:1–16.

115. Elder, G.A. 2015. Update on TBI and Cognitive Impairment in Military Veterans. *Curr. Neurol. Neurosci. Rep.* 15:1–9.

116. Hyder, A.A., C.A. Wunderlich, P. Puvanachandra, G. Gururaj, and O.C. Kobusingye. 2007. The impact of traumatic brain injuries: A global perspective. *NeuroRehabilitation*. 22:341–353.

117. Cloots, R.J.H., J.A.W. Van Dommelen, T. Nyberg, S. Kleiven, and M.G.D. Geers. 2011. Micromechanics of diffuse axonal injury: Influence of axonal orientation and anisotropy. *Biomech. Model. Mechanobiol.* 10:413–422.

118. Elkin, B.S., and B. Morrison. 2007. Region-specific tolerance criteria for the living brain. *Stapp Car Crash J.* 51:127–138.

119. Morrison, B., H.L. Cater, C.C.-B. Wang, F.C. Thomas, C.T. Hung, G.A. Ateshian, and L.E. Sundstrom. 2003. A tissue level tolerance criterion for living brain developed with an in vitro model of traumatic mechanical loading. *Stapp Car Crash J.* 47:93–105.

120. Tang-Schomer, M.D., A.R. Patel, P.W. Baas, and D.H. Smith. 2010. Mechanical breaking of microtubules in axons during dynamic stretch injury underlies delayed elasticity, microtubule disassembly, and axon degeneration. *FASEB J.* 24:1401–

1410.

121. Knutsen, A.K., A.D. Gomez, M. Gangolli, W.-T. Wang, D. Chan, Y.-C. Lu, E. Christoforou, J.L. Prince, P. V. Bayly, J.A. Butman, and D.L. Pham. 2020. In vivo estimates of axonal stretch and 3D brain deformation during mild head impact. *Brain Multiphysics*. 100015.

122. Sullivan, S., S.A. Eucker, D. Gabrieli, C. Bradfield, B. Coats, M.R. Maltese, J. Lee, C. Smith, and S.S. Margulies. 2015. White matter tract-oriented deformation predicts traumatic axonal brain injury and reveals rotational direction-specific vulnerabilities. *Biomech. Model. Mechanobiol.* 14:877–896.

123. Wright, R.M., and K.T. Ramesh. 2012. An axonal strain injury criterion for traumatic brain injury. *Biomech. Model. Mechanobiol.* 11:245–260.

124. Chatelin, S., C. Deck, F. Renard, S. Kremer, C. Heinrich, J.P. Armspach, and R. Willinger. 2011. Computation of axonal elongation in head trauma finite element simulation. *J. Mech. Behav. Biomed. Mater.* 4:1905–1919.

125. Colgan, N.C., M.D. Gilchrist, and K.M. Curran. 2010. Applying DTI white matter orientations to finite element head models to examine diffuse TBI under high rotational accelerations. *Prog. Biophys. Mol. Biol.* 103:304–309.

126. Giordano, C., S. Zappalà, and S. Kleiven. 2017. Anisotropic finite element models for brain injury prediction: the sensitivity of axonal strain to white matter tract inter-subject variability. *Biomech. Model. Mechanobiol.* 16:1269–1293.

127. Hajiaghamemar, M., T. Wu, M.B. Panzer, and S.S. Margulies. 2020. Embedded axonal fiber tracts improve finite element model predictions of traumatic brain injury. *Biomech. Model. Mechanobiol.* 19:1109–1130.

128. Cinelli, I., M. Destrade, P. McHugh, and M. Duffy. 2018. Effects of nerve bundle geometry on neurotrauma evaluation. *Int. j. numer. method. biomed. eng.* 34.

129. Cullen, D.K., and M.C. LaPlaca. 2006. Neuronal Response to High Rate Shear Deformation Depends on Heterogeneity of the Local Strain Field. *J. Neurotrauma*. 23:1304–1319.

130. Singh, A., S. Kallakuri, C. Chen, and J.M. Cavanaugh. 2009. Structural and functional changes in nerve roots due to tension at various strains and strain rates: An in-vivo study. *J. Neurotrauma*. 26:627–640.

131. Lu, Y.-B., K. Franze, G. Seifert, C. Steinhauser, F. Kirchhoff, H. Wolburg, J. Guck, P. Janmey, E.-Q. Wei, J. Kas, and A. Reichenbach. 2006. Viscoelastic properties of individual glial cells and neurons in the CNS. *Proc. Natl. Acad. Sci.* 103:17759–17764.

132. Grevesse, T., B.E. Dabiri, K.K. Parker, and S. Gabriele. 2015. Opposite rheological properties of neuronal microcompartments predict axonal vulnerability in brain injury. *Sci. Rep.* 5:9475.

133. Brown, N.J., R.C. Mannix, M.J. O'Brien, D. Gostine, M.W. Collins, and W.P. Meehan. 2014. Effect of cognitive activity level on duration of post-concussion symptoms. *Pediatrics*. 133:e299-304.

134. Ray, A., O. Lee, Z. Win, R.M. Edwards, P.W. Alford, D.H. Kim, and P.P. Provenzano. 2017. Anisotropic forces from spatially constrained focal adhesions mediate contact guidance directed cell migration. *Nat. Commun.* 8:1–17.

135. Win, Z., G.D. Vrla, K.E. Steucke, E.N. Sevcik, E.S. Hald, and P.W. Alford. 2014. Smooth muscle architecture within cell-dense vascular tissues influences functional

contractility. *Integr. Biol. (United Kingdom)*. 6:1201–1210.

136. Win, Z., J.M. Buksa, and P.W. Alford. 2018. Architecture-Dependent Anisotropic Hysteresis in Smooth Muscle Cells. *Biophys. J.* 115:2044–2054.

137. Bursac, N., K.K. Parker, S. Iravanian, and L. Tung. 2002. Cardiomyocyte cultures with controlled macroscopic anisotropy: a model for functional electrophysiological studies of cardiac muscle. *Circ. Res.* 91.

138. Teravskis, P.J., A. Covelo, E.C. Miller, B. Singh, H.A. Martell-Martínez, M.A. Benneyworth, C. Gallardo, B.R. Oxnard, A. Araque, M.K. Lee, and D. Liao. 2018. A53T Mutant Alpha-Synuclein Induces Tau-Dependent Postsynaptic Impairment Independently of Neurodegenerative Changes. *J. Neurosci.* 38:9754–9767.

139. Nakayama, Y., Y. Aoki, and H. Niitsu. 2001. Studies on the Mechanisms Responsible for the Formation of Focal Swellings on Neuronal Processes Using a Novel *In Vitro* Model of Axonal Injury. *J. Neurotrauma*. 18:545–554.

140. Ahmadzadeh, H., D.H. Smith, and V.B. Shenoy. 2015. Mechanical Effects of Dynamic Binding between Tau Proteins on Microtubules during Axonal Injury. *Biophys. J.* 109:2328–37.

141. Stemper, B.D., A.S. Shah, R. Chiariello, C.M. Olsen, M.D. Budde, A. Glavaski-Joksimovic, M. McCrea, S.N. Kurpad, and F.A. Pintar. 2016. Prediction of Post-Concussive Behavioral Changes in a Rodent Model Based on Head Rotational Acceleration Characteristics. *Ann. Biomed. Eng.* 44:3252–3265.

142. Stemper, B.D., A.S. Shah, F.A. Pintar, M. McCrea, S.N. Kurpad, A. Glavaski-Joksimovic, C. Olsen, and M.D. Budde. 2015. Head Rotational Acceleration Characteristics Influence Behavioral and Diffusion Tensor Imaging Outcomes

Following Concussion. *Ann. Biomed. Eng.* 43:1071–1088.

143. Rowson, S., and S.M. Duma. 2013. Brain injury prediction: Assessing the combined probability of concussion using linear and rotational head acceleration. *Ann. Biomed. Eng.* 41:873–882.

144. Ji, S., W. Zhao, Z. Li, and T.W. McAllister. 2014. Head impact accelerations for brain strain-related responses in contact sports: a model-based investigation. *Biomech. Model. Mechanobiol.* 13:1121–1136.

145. Asken, B.M., S.T. DeKosky, J.R. Clugston, M.S. Jaffee, and R.M. Bauer. 2018. Diffusion tensor imaging (DTI) findings in adult civilian, military, and sport-related mild traumatic brain injury (mTBI): a systematic critical review. *Brain Imaging Behav.* 12:585–612.

146. Cnossen, M.C., E.A. Winkler, J.K. Yue, D.O. Okonkwo, A.B. Valadka, E.W. Steyerberg, H.F. Lingsma, G.T. Manley, K. Dams-O'Connor, W.A. Gordon, A.J. Hricik, A.I.R. Maas, D.K. Menon, P. Mukherjee, A.M. Puccio, D.M. Schnyer, M.J. Vassar, and E.L. Yuh. 2017. Development of a Prediction Model for Post-Concussive Symptoms following Mild Traumatic Brain Injury: A TRACK-TBI Pilot Study. *J. Neurotrauma*. 34:2396–2408.

147. Ye, G.J.C., Y. Aratyn-Schaus, A.P. Nesmith, F.S. Pasqualini, P.W. Alford, and K.K. Parker. 2014. The contractile strength of vascular smooth muscle myocytes is shape dependent. *Integr. Biol.* 6:152–163.

148. Win, Z., J.M. Buksa, K.E. Steucke, G.W. Gant Luxton, V.H. Barocas, and P.W. Alford. 2017. Cellular Microbiaxial Stretching to Measure a Single-Cell Strain Energy Density Function. *J. Biomech. Eng.* 139:071006.

149. Steucke, K.E., Z. Win, T.R. Stemler, E.E. Walsh, J.L. Hall, and P.W. Alford. 2017. Empirically determined vascular smooth muscle cell mechano-adaptation law. *J. Biomech. Eng.* 139.

150. Rothermel, T.M., Z. Win, and P.W. Alford. 2020. Large-deformation strain energy density function for vascular smooth muscle cells. *J. Biomech.* 111:110005.

151. Villegas, M., Z. Cetinic, A. Shakeri, and T.F. Didar. 2018. Fabricating smooth PDMS microfluidic channels from low-resolution 3D printed molds using an omniphobic lubricant-infused coating. *Anal. Chim. Acta*. 1000:248–255.

152. Steucke, K.E., P. V. Tracy, E.S. Hald, J.L. Hall, and P.W. Alford. 2015. Vascular smooth muscle cell functional contractility depends on extracellular mechanical properties. *J. Biomech.* 48:3044–3051.

153. Alford, P.W., A.P. Nesmith, J.N. Seywerd, A. Grosberg, and K.K. Parker. 2011. Vascular smooth muscle contractility depends on cell shape. *Integr. Biol.* 3:1063–1070.